Rolling Contact Fatigue of Railway Wheel without defect

Médiateur Nemeyuko

Rolling Contact Fatigue of Railway Wheel without defect

Dr. Médiateur NEMEYUKO*

*Expleo France

July 1, 2025

Abstract

Rolling Contact Fatigue (RCF) is a highly localized damage phenomenon that can occur in railway wheels subjected to multiaxial, non-proportional cyclic loads. In such scenarios, cracks are initiated either at the surface or beneath it. Repeated cyclic tangential forces primarily cause surface-initiated cracks during wheel-rail interactions, which lead to cumulative plastic deformation of the surface material. This contact can be either between the wheel flange and the rail flange for low values of the coefficient of friction during the traction phases, or between the wheel tread and the rail head for high values of the coefficient of friction during the braking phases. The high energy efficiency of rail transportation is made possible by the favorably low losses in the rolling contact between the hard surfaces of wheel and rail, which meet only in a very small contact zone of relatively elliptical shape. In this article, a two-dimensional cross-section of a defect-free railway wheel was modeled using Abaqus computational software. The elastoplastic material model proposed by Lemaitre and Chaboche with a behavior law combining isotropic strain hardening and nonlinear kinematic strain hardening was adopted. Random changes in stress and strain state lead to multiaxial fatigue behavior. The wheel damage is thus obtained by calculating the value of the fatigue parameter, FP, in different planes of the material using the Jiang-Sehitoglu multiaxial fatigue approach. The model for predicting fatigue life at crack initiation in the wheel is based on a combination of the Smith-Watson-Topper relationship and the Jiang-Sehitoglu fatigue parameter. The maximum fatigue parameter corresponds to the critical plane at which fatigue cracks initiate. Wheel-rail contact, elastoplastic model, isotropic strain hardening and nonlinear kinematic strain hardening, critical plane, elastic shakedown, plastic shakedown, ratcheting phenomenon, fatigue damage, and fatigue life.

Keywords: wheel-rail contact, elastoplastic model, isotropic strain hardening, nonlinear kinematic strain hardening, critical plane, fatigue damage, fatigue life.

1 Introduction

Rolling contact fatigue is the degradation of contact materials, such as wheels and rails, due to repeated cyclic loading. This major problem in the rail industry can lead to premature failures, serious accidents, and high maintenance costs. This paper presents a robust approach to predicting the fatigue life of railway wheels using a two-dimensional method. A 2D finite element model of a defect-free wheel is used to capture stress and strain histories, taking into account tangential forces caused by wheel-rail friction. The model incorporates an elastoplastic behavior law that combines isotropic and nonlinear kinematic strain hardening. The results of the finite element analysis are integrated into the Jiang-Sehitoglu multiaxial fatigue model, which is based on an energy density and critical plane approach. This model, combined with the Smith-Watson-Topper criterion, is used to estimate the fatigue life of wheels and rails subjected to complex loading [1].

Factors such as load and friction levels have a significant impact on stress and strain distribution, as well as on component damage and service life [1]. High levels can accelerate wear and increase the risk of damage such as shelling and spalling. In addition, subsurface cracks are often caused by pre-existing macroscopic defects in the material, which act as stress concentration points [2].

Wheel fractures caused by crack propagation can have serious consequences, including derailment. Periodic inspections and preventive maintenance are essential to detect and prevent such failures [2]. Rolling contact fatigue models must take into account both actual geometric contact conditions and material properties, including possible defects, to provide more accurate predictions [1] [2]. It is important to note that methods based on uniaxial tensile loading data may not be directly applicable to the analysis of rolling contact behavior [1].

To validate the numerical model of wheel-rail contact, I adopted a methodical and rigorous approach inspired by the seminal work of Hertz (1881) and Johnson (1987). Hertz's contact theory allowed for an initial load to be without consideration of friction in the case of pure rolling [3]. I then investigated the influence of load level variations on wheel life [4]. Using the finite element method, I was able to accurately model a wheel section to better understand its mechanical behavior [5]. I initially ignored the defects present in the wheel, before introducing them for a more complete fatigue analysis [6]. Finally, the construction of the shakedown map will allow the identification of the safest loading conditions to ensure the durability of railway wheels [7].

2 Multiaxial fatigue criterion

The Jiang-Sehitoglu fatigue criterion is an approach used to evaluate the number of cycles to failure N_f required to initiate fatigue cracks in materials subjected to cyclic loading. This criterion is based on the fatigue parameter FP, which is a weighted sum of the energies associated with the tensile-compressive ($\langle\sigma_{max}\rangle\ \Delta\varepsilon_p$) and shear ($\Delta\tau\ \Delta\gamma_p$) stresses experienced by the material. This fatigue parameter is given by the following relationship:

$$FP = \langle\sigma_{max}\rangle \frac{\Delta\varepsilon_p}{2} + J\Delta\tau\Delta\gamma_p \tag{1}$$

where σ_{max}, with $\langle . \rangle = \max(., 0)$, is the maximum normal stress on the crack plane, $\Delta\tau$ the shear stress variation in the crack plane. $\Delta\varepsilon_p$ and $\Delta\gamma_p$ are the tensile-compressive plastic strain amplitude at the crack plane and the shear plastic strain amplitude in the crack plane, respectively. The first term of the fatigue parameter FP corresponds to the tensile component of the damage in mode I (opening mode). The second term corresponds to the shear component of mode II damage - a shear mode in which J is a weighting parameter. The value of J was set to 0.2, as in other studies [8] [9] [10].

The fatigue crack initiation life prediction model is based on a combination of the Smith-Watson-Topper relationship and the Jiang-Sehitoglu maximum fatigue parameter, and is given by the following relationship:

$$FP_{max} = \frac{\sigma_f^2}{E} (2N_f)^{2b'} + \sigma_f \varepsilon_f (2N_f)^{b'+c'} \tag{2}$$

As part of the finite element analysis, stress and strain histories are collected for all relevant integration points at each time increment during the stabilized cycle. These data are used to characterize the mechanical behavior of the material at different times during the loading cycle. For each integration point, normal and shear stresses and strains are determined on a plane of the material with an orientation angle α with respect to axis 1, as shown in the Fig. 1. This approach provides a complete representation of the stress and strain states in the material, taking into account the orientation of the planes with respect to the principal direction of loading.

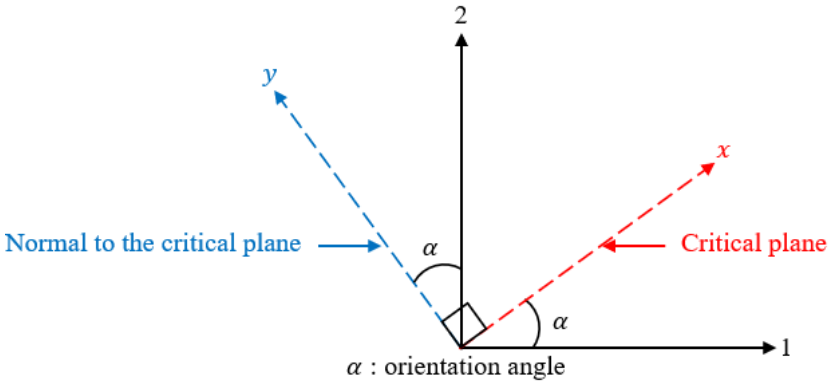

Figure 1: Definition of a critical plane orientation angle α for the calculation of the maximum fatigue parameter $FP_{\max}$.

By collecting these data at each time increment during the stabilized cycle, it is possible to reconstruct the evolution of stresses and strains in the wheels and rails over time. This provides essential information for assessing the mechanical performance of the material and predicting its fatigue life under real-life conditions, especially taking into account the tangential forces caused by wheel-rail friction. To calculate the normal (σ_{xx} and σ_{yy}) and shear (τ_{xy}) stresses on any plane in a wheel section element, the following equations can be used, varying the orientation angle α of each material plane:

$$\begin{aligned}
\sigma_{\mathrm{xx}} &= \sigma_{11}\,\cos^2\alpha + \sigma_{22}\,\sin^2\alpha + 2\tau_{12}\,\cos\alpha\,\sin\alpha \\
\sigma_{\mathrm{yy}} &= \sigma_{11}\,\sin^2\alpha + \sigma_{22}\,\cos^2\alpha - 2\tau_{12}\,\cos\alpha\,\sin\alpha \\
\tau_{\mathrm{xy}} &= -\sigma_{11}\,\cos\alpha\,\sin\alpha + \sigma_{22}\cos\alpha\,\sin\alpha + \tau_{12}(\cos\alpha^2 - \sin\alpha^2)
\end{aligned} \tag{3}$$

This allows a complete characterization of the stress states in the material, taking into account the orientation of the planes with respect to the principal directions of loading. Similarly, the strain components as a function of the α angle can be expressed as follows:

$$\begin{aligned}
\varepsilon_{\mathrm{xx}} &= \varepsilon_{11}\,\cos^2\alpha + \varepsilon_{22}\,\sin^2\alpha + 2\gamma_{12}\,\cos\alpha\,\sin\alpha \\
\varepsilon_{\mathrm{yy}} &= \varepsilon_{11}\,\sin^2\alpha + \varepsilon_{22}\,\cos^2\alpha - 2\gamma_{12}\,\cos\alpha\,\sin\alpha \\
\gamma_{\mathrm{xy}} &= -\varepsilon_{11}\,\cos\alpha\,\sin\alpha + \varepsilon_{22}\cos\alpha\,\sin\alpha + \gamma_{12}(\cos^2\alpha - \sin^2\alpha)
\end{aligned} \tag{4}$$

The maximum normal stress is defined by $\sigma_{\max} = \max(\sigma_{\mathrm{yy}})$.

The shear stress variation in each plane of the material is the difference between the maximum and minimum shear stresses and is calculated as follows:

$$\Delta\tau = \max(\tau_{\mathrm{xy}}) - \min(\tau_{\mathrm{xy}}) \tag{5}$$

where $\max(\tau_{xy})$ and $\min(\tau_{xy})$ are the maximum and minimum shear stresses in the α plane.

Similarly, the normal and shear strain variations on each plane of the material are given by the following equations:

$$\Delta\varepsilon = \max(\varepsilon_{yy}) - \min(\varepsilon_{yy}) \tag{6}$$
$$\Delta\gamma = \max(\gamma_{xy}) - \min(\gamma_{xy}) \tag{7}$$

These expressions of maximum normal stress on the crack plane, normal strain variation on the crack plane, stress variation and shear strain in the crack plane can be determined explicitly on stress-strain curves obtained from numerical simulations, as shown in the Fig. 2. The $\Delta\varepsilon_p$ and $\Delta\gamma_p$ variations shown in this figure are measured on recordings in the most damaged element. The $\Delta\varepsilon_p$ and $\Delta\gamma_p$ are used in the calculation of the fatigue damage parameter $FP_{\max}$.

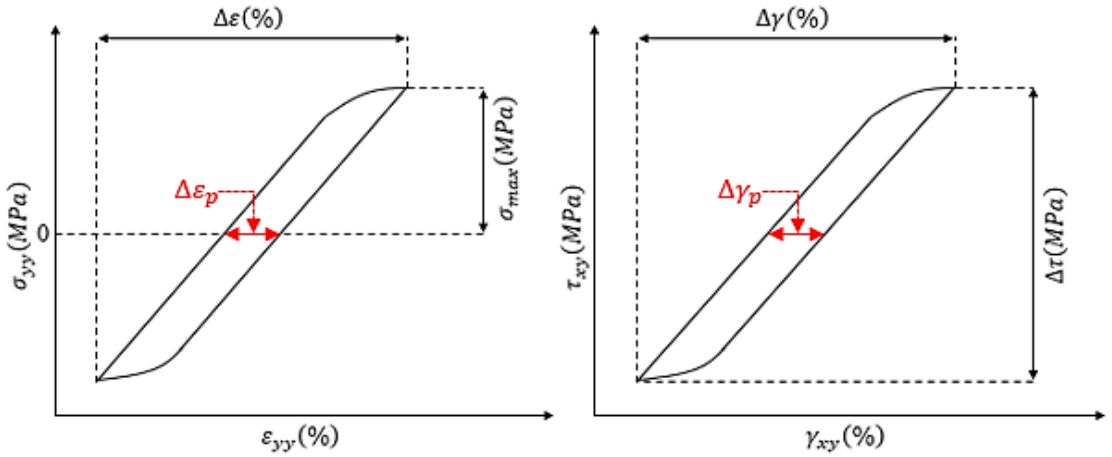

Figure 2: Procedure for determining the stresses and strains that contribute to the FCR damage calculation. These minimum and maximum stress and strain values are calculated during the last load cycle.

3 Plasticity model

The kinematic strain hardening plasticity model is used to simulate the plastic behavior of materials under cyclic loading. It is characterized by the yield function and the plasticity criterion.

The yield function f determines the behavior of the material:

- $f < 0$: elastic behavior;
- $f = 0$ and $\frac{df}{dt} = 0$: plastic flow or plasticity threshold, potential plastic deformation;
- $f = 0$ and $\frac{df}{dt} < 0$: elastic unloading.

The plasticity criterion is expressed by :

$$f(\sigma - X) - R - \sigma_0 = 0 \tag{8}$$

where σ is the Cauchy stress tensor, X is the kinematic strain hardening tensor, R is the isotropic strain hardening scalar, and σ_0 is the yield stress.

The equivalent Von Mises stress, σ_{eq}, is calculated by :

$$\sigma_{eq} = \sqrt{\frac{3}{2}(\sigma - X) : (\sigma - X)} \tag{9}$$

The von Mises equivalent stress is a fundamental measure in mechanics of materials for evaluating yield strength under multiaxial loading. Although the equation (9) gives a generalized form with tensor X, the historical formulation by von Mises (1913) corresponds to a special case where $X = 0$. For a ductile isotropic material, the equivalent Von Mises stress is expressed as a function of the principal stresses σ_1, σ_2, σ_3 by :

$$\sigma_{\text{eq}} = \sqrt{\frac{1}{2}\left[(\sigma_1 - \sigma_2)^2 + (\sigma_2 - \sigma_3)^2 + (\sigma_1 - \sigma_3)^2\right]} \tag{10}$$

This expression represents the critical strain energy that causes plasticity.

The form $\sigma_{eq} = \sqrt{\frac{3}{2}(\sigma - X) : (\sigma - X)}$ generalizes the classical criterion:
- X corresponds to an internal stress tensor.
- The doubly contracted product $(\sigma - X) : (\sigma - X)$ is equivalent to the trace of the deviator tensor squared.

The standard case ($X = 0$) describes isotropic plasticity, which is widely used for steel. On the other hand, the case with $X \neq 0$ models advanced effects such as initial anisotropy. Kinematic strain hardening is a plasticity model with translation of the center of the loading surface. The criterion shows excellent agreement with tensile-torsion tests for ductile metals, with an accuracy of $\pm$ 5 % compared to Tresca. In pure shear, it predicts an elastic limit at $\sigma_e/\sqrt{3}$, which is confirmed by tests. This generalization makes it possible to adapt the original criterion to complex materials and loads, while retaining its fundamental energetic interpretation.

The Von Mises Equivalent Stress Potential calculates a single measure of the stress state from the stress tensor σ and the internal stress X, facilitating the analysis and modeling of the plastic behavior of the material. The Von Mises Equivalent Stress Potential is defined by :

$$f(\sigma - X) = \sqrt{\frac{3}{2}(S - X') : (S - X')} \tag{11}$$

where S is the stress tensor deviator, defined as the part of the stress tensor that represents the stress without the hydrostatic pressure component. Mathematically, it is defined by $S = \sigma + pI$, where p is the hydrostatic pressure and I is the identity tensor. The S deviator is used to characterize the stresses that contribute to deformation, independent of the uniform pressure in all directions. Similarly, the deviator of the internal stress tensor is defined as the part of the internal stress tensor that represents the internal stresses without the hydrostatic pressure component. If X is the internal stress tensor, then $X^{'}$ is its deviator. This makes it possible to isolate the specific contributions of kinematic strain hardening without the influence of hydrostatic pressure.

Plastic flow is considered to be associated with the plastic strain rate normal to the loading surface:

$$\dot{\varepsilon}_{pl} = \dot{\bar{\varepsilon}}_{pl} \frac{\partial f}{\partial \sigma} \tag{12}$$

where $\dot{\varepsilon}_{pl}$ is the plastic strain rate tensor and $\dot{\bar{\varepsilon}}_{pl}$ is the equivalent plastic strain rate.

The evolution of the equivalent plastic strain is given by :

$$\sigma_0 \dot{\bar{\varepsilon}}_{pl} = \sigma : \dot{\varepsilon}_{pl} \tag{13}$$

In the context of isotropic Von Mises plasticity, it can be expressed as :

$$\dot{\bar{\varepsilon}}_{pl} = \sqrt{\frac{2}{3}\dot{\varepsilon}_{pl} : \dot{\varepsilon}_{pl}} \tag{14}$$

This model provides an accurate description of the plastic behavior of materials under cyclic loading, taking into account kinematic strain hardening and the evolution of the yield surface.

4 Hardening law

Hardening laws in the mechanics of materials focus on two main variables such as:

- the tensor variable X, which represents the center of the elastic domain in stress space and describes its translation.
- the scalar variable R, which represents the elastic domain's size change.

Hardening models include linear kinematic hardening, where the hardening modulus remains constant regardless of the amplitude of plastic deformation, and the combined model, which is the sum of isotropic and nonlinear kinematic hardening. Nonlinear kinematic strain hardening describes the nonlinear translation of the yield surface, while isotropic strain hardening describes the variation in the size of the yield surface. Prager's law is improved by introducing an $-\gamma X\dot{\bar{\varepsilon}}^{pl}$-recall term that adds an evanescent memory effect to the deformation path. This approach allows for more accurate modeling of the plastic behavior of materials, especially under cyclic loading or large plastic deformations.

The nonlinear kinematic strain hardening law is a linear combination of two terms: a purely kinematic term and a recall term that introduces nonlinearity. Therefore, the strain-hardening law is defined as follows:

$$\dot{X} = C\frac{1}{\sigma^0}(\sigma - X)\dot{\bar{\varepsilon}}^{pl} - \gamma X\dot{\bar{\varepsilon}}^{pl}, \tag{15}$$

The first term $C\frac{1}{\sigma^0}(\sigma - X)\dot{\bar{\varepsilon}}^{pl}$ represents the kinematic hardening of the material. It is proportional to the difference between the applied stress σ and the internal stress X, multiplied by the plastic strain rate $\dot{\bar{\varepsilon}}^{pl}$. The parameter C is the initial kinematic strain hardening modulus, which determines the initial response of the material to kinematic hardening. The quantity σ^0 is the equivalent stress that defines the size of the yield surface. This term describes the material's response to plastic deformation in terms of hardening. The second term $-\gamma X\dot{\bar{\varepsilon}}^{pl}$ represents the restoring term that introduces nonlinearity into the strain-hardening law. It is proportional to the internal stress X and the plastic strain rate $\dot{\bar{\varepsilon}}^{pl}$. The parameter γ determines the rate at which the kinematic hardening modulus decreases with increasing plastic strain. This term models the evanescent memory effect of the deformation path. When C and γ are zero, the model reduces to isotropic strain-hardening. When γ is zero, we find a linear kinematic strain-hardening model.

The kinematic strain-hardening law consists of two main components: the deviatoric part and the hydrostatic part. The deviatoric part is the only one that influences the behavior of the material, as it is associated with variations in deviatoric stress. This type of stress measures changes in the material's shape without affecting its overall volume. The deviatoric part specifically describes how the material hardens in response to plastic deformation. In contrast, the hydrostatic part relates to changes in hydrostatic stress, which measures changes in the material's volume. This component typically does not impact the plastic behavior of the material, since volume changes do not contribute to its hardening. As a result, only the deviatoric part of the kinematic strain-hardening law is taken into account when analyzing plastic behavior.

The isotropic strain-hardening law describes how the yield surface size (σ^0) evolves as a function of equivalent plastic strain ($\bar{\varepsilon}^{pl}$). This evolution is often modeled by an exponential law:

$$\sigma^0 = \sigma|_0 + Q_\infty(1 - e^{-b\bar{\varepsilon}^{pl}}) \tag{16}$$

Where $\sigma|_0$ represents the initial yield strength at zero plastic strain, Q_∞ denotes the maximum variation in yield surface size, and b is the parameter that defines the rate of change in yield surface size with respect to plastic strain. If the size of the yield surface remains constant, the model simplifies to nonlinear kinematic strain hardening. However, if the size of the yield surface changes according to an exponential law, it introduces isotropic strain hardening, which alters the overall strength of the material. The evolution of isotropic and kinematic nonlinear strain-hardening components is depicted in the Fig. 3 for unidirectional loading and in the Fig. 4 for multiaxial loading.

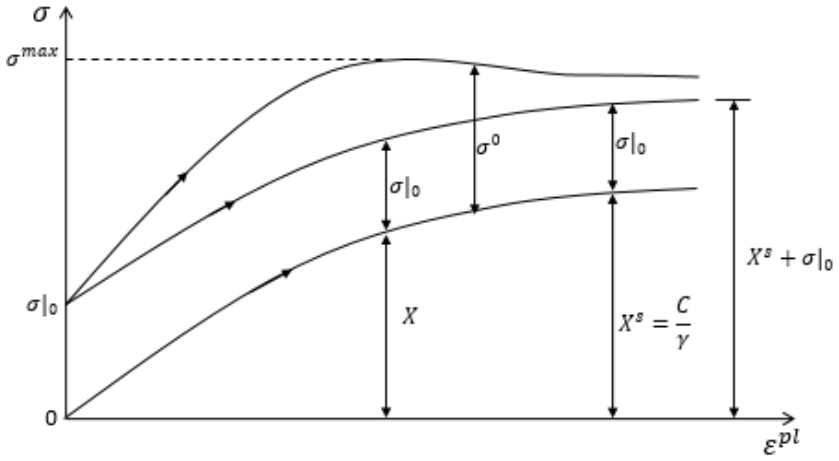

Figure 3: Unidirectional representation of a nonlinear kinematic isotropic strain-hardening model [11].

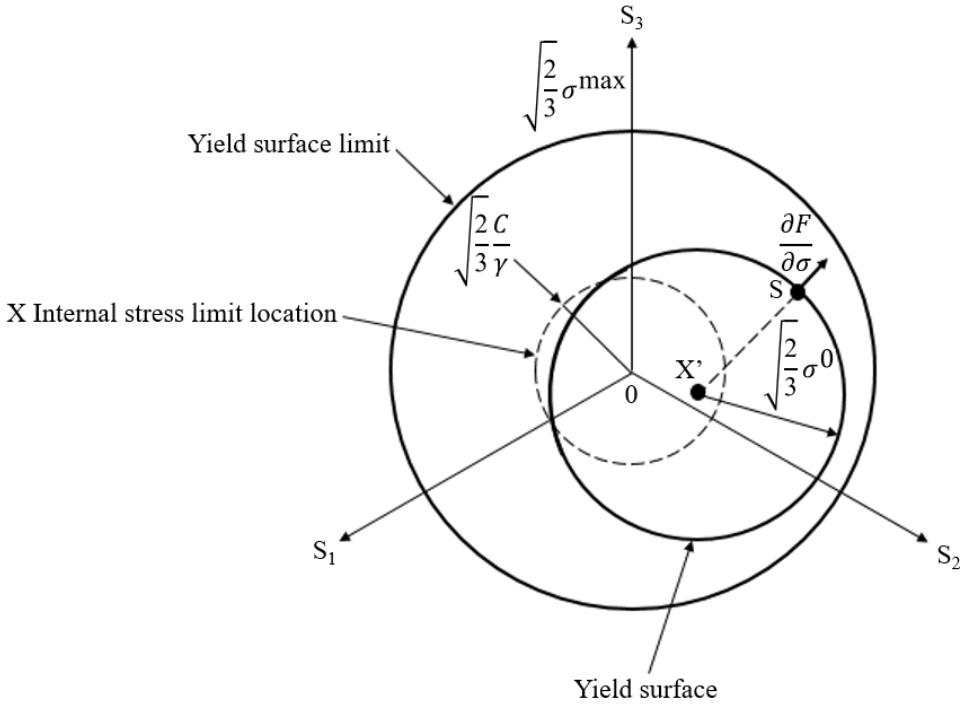

Figure 4: Three-dimensional representation of a nonlinear kinematic isotropic strain-hardening model [11].

In the context of the nonlinear kinematic strain-hardening component, the internal stress X is confined within a cylinder of radius $\sqrt{\frac{2}{3}}X^s = \sqrt{\frac{2}{3}}\frac{C}{\gamma}$, where X^s represents the value of X at saturation, which occurs during significant plastic deformations. This indicates that all stress points must lie within a cylinder with a radius of $\sqrt{\frac{2}{3}}\sigma^{\max}$, as the yield surface is constrained. For large plastic deformations, each stress point is contained within a cylinder of radius $\sqrt{\frac{2}{3}}(X^s + \sigma^s)$, where σ^s is the equivalent stress that determines the size of the yield surface at these high levels of plastic deformation. For the isotropic component, σ^s is defined as the last value used to establish the size of the yield surface :

$$\sigma^s = \sigma|_0 + Q_\infty \tag{17}$$

The term σ^s refers to the sum of the yield strength at zero plastic strain, denoted as $\sigma|_0$, and the maximum variation in the size of the yield surface, represented by Q_∞. In simpler terms, σ^s indicates the maximum stress that a material can endure before the size of the yield surface reaches its maximum limit during large plastic deformations.

The isotropic and nonlinear kinematic strain-hardening model combines two types of strain-hardening to accurately characterize the plastic behavior of materials under cyclic loading. The isotropic strain-hardening models the evolution of the material's resistance to plastic deformation as a function of accumulated plastic strain, which represents the change in size of the yield surface (σ_0). This strain-hardening can be nonlinear to capture the phenomenon of strain-hardening saturation, as described by the equation (16). On the other hand, nonlinear kinematic strain-hardening describes the translation of the yield surface in stress space (one- or three-dimensional) and is quantified by the internal stress tensor (X), as illustrated in the figures 3 and 4. The relationship between accumulated plastic strain and the shift of the yield surface is nonlinear [12] and is modeled by the following tensor equation:

$$\dot{X} = \frac{2}{3}C\dot{\varepsilon}^p - \gamma X\dot{p} \tag{18}$$

where C and γ are the material parameters, and p is the cumulative plastic strain. This equation is equivalent to the equation (15).

5 Numerical modeling

The defect-free railway wheel section was modeled in 2D using Abaqus Standard to analyze its mechanical behavior under cyclic loading. The model, with dimensions of $200\times100\text{mm}^2$, uses CPE8R finite elements (eight-node quadrilaterals with reduced integration) to accurately capture stresses and strains during in-plane deformation. The wheel is subjected to a normal load F, which is applied through a moving Hertzian contact pressure, simulating a complete cycle (from 0 to 1 second) that corresponds to one wheel revolution. A DLOAD subroutine was utilized to precisely define the spatial and temporal evolution of this load. Boundary conditions were set, with zero displacement u_x on the lateral edges and zero u_y on the lower edge, to maintain a plane deformation state. Convergence analyses were conducted to validate the model's robustness and accuracy, ensuring a reliable simulation of the mechanical behavior of railway wheels under realistic loading conditions.

To accurately model the contact between wheels and rails, we assume that both dimensions are infinite. This eliminates edge effects that could distort the results and more accurately reflects real-world loading conditions. While the cylinder-plane contact model is sometimes used, representing the interaction between two cylinders with perpendicular axes, considering the elliptical shape of the contact surface provides a more accurate characterization of the stress and strain distribution. This approach is crucial for evaluating the mechanical behavior of the system effectively. In wheel-rail contact, the contact zone typically has dimensions a and b that are generally less than 10 mm, which is very small compared to the radii of curvature of the wheel (0.3 m) and rail (0.445 m). Moreover, according to Hertz's theory, the maximum pressure in this contact area can often reach up to 1 GPa [13]. These conditions validate the assumptions of Hertz's contact theory and justify its application to model railway systems.

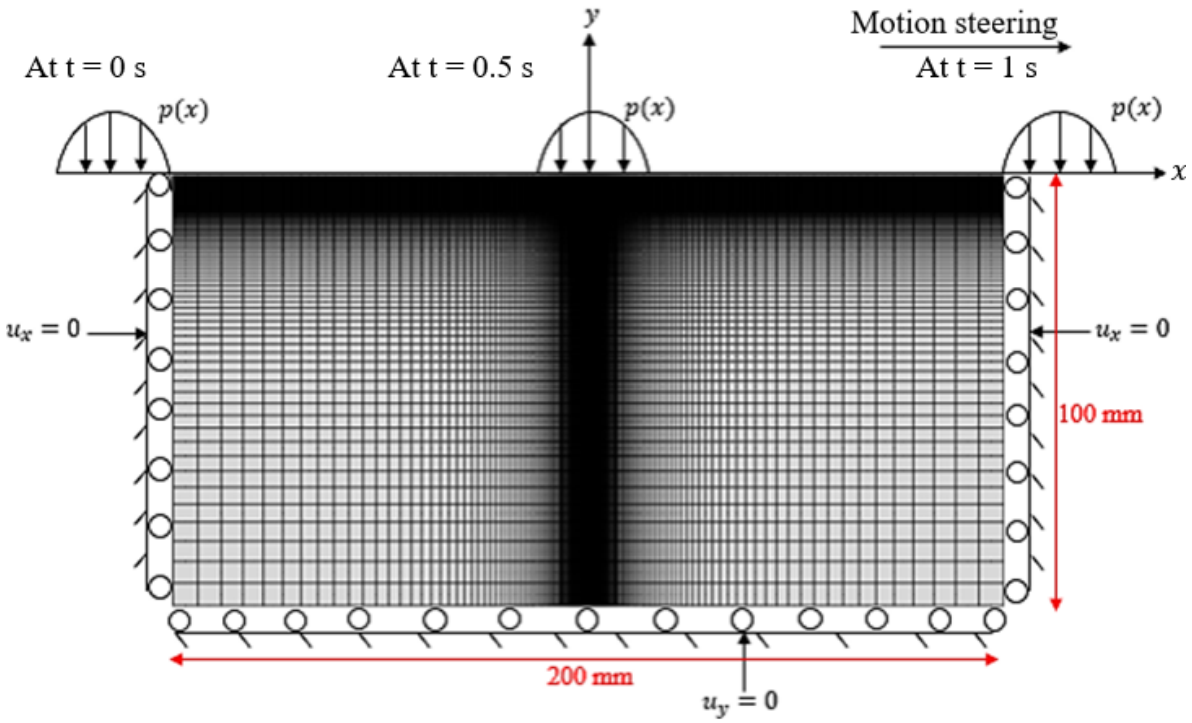

Figure 5: Two-dimensional model of a defect-free railway wheel section subjected to moving Hertzian contact pressure [11].

5.1 Hertz's Contact Theory

The wheel-rail contact is assumed to be linear. This approach is often used to model wheel-rail contact as a first approximation. It assumes that the wheel-rail contact can be approximated by a contact between a cylinder (the wheel) and a plane (the rail), which is linear. In this case, the contact pressure is distributed semi-elliptically along the contact length $2a$ and varies in the direction x under normal load. This pressure distribution is commonly described by the Hertz contact theory, which is considered a valid approximation for elastic deformations in homogeneous and isotropic materials.

The contact pressure is expressed as follows [3] :

$$p(x,t) = p_0\sqrt{1 - \frac{[x - x_0(t)]^2}{a^2}} \quad \forall x \in [x_0 - a, x_0 + a] \tag{19}$$

where

$$x_0(t) = -\frac{L}{2} + Vt, \tag{20}$$

Otherwise,

$$p(x,t) = 0 \tag{21}$$

Let $x_0(t)$ represent the position of the center of the contact zone as a function of time, and let p_0 denote the maximum contact pressure, which is given by the following expression:

$$p_0 = \sqrt{\frac{FE^*}{\pi R}} \tag{22}$$

and a is the half-length of the contact zone, which can be expressed using the following relationship :

$$a = \sqrt{\frac{FR}{\pi E^*}} \tag{23}$$

where F represents the normal force per unit length, R is the idealized radius of curvature of the rail and E^* denotes the effective Young's modulus of the material, which is given by the following relationship:

$$E^* = \frac{E}{2(1-\nu^2)} \tag{24}$$

where E represents the Young's modulus of the materials used for the wheel and rail.

For tangential loading, the contact pressure $q(x,t)$ is calculated by multiplying the normal contact pressure by the coefficient of friction μ as follows:

$$q(x,t) = \mu p(x,t) = \mu p_0 \sqrt{1 - \frac{[x - x_0(t)]^2}{a^2}} \tag{25}$$

Therefore, this tangential contact pressure is also distributed in a semi-elliptical shape along the contact length.

The table 1 presents values for the force exerted on the wheel or rail per unit length, the maximum contact pressure, and the half-length of the contact zone in the case of linear wheel-rail contact. These values are useful for defining contact conditions when modeling the behavior of wheel-rail systems in numerical simulations or theoretical analyses.

F (MN/m)	p_0 (MPa)	a (mm)
4	697.5	3.7
7	922.8	5.8
12	1208.2	6.3
18	1479.7	7.7
22	1635.9	8.6

Table 1: Conditions of linear contact between the wheel and the rail.

During braking, the coefficient of friction (μ) is positive, indicating a force that opposes movement. In contrast, during traction or rolling without sliding, μ is negative, which acts in favor of movement. When the vehicle is stationary, the contact area between the wheel and the rail is determined by three key factors:

- Rail geometry: The rounded shape of the rail head directly influences the configuration of the contact zone.
- Wheel profile: Wheels are often designed with a conical or slightly domed shape to adapt to the rail profile, as shown in the figure 6.
- Elasticity of materials: The elastic deformation of both the rail and the wheel under the vehicle's weight helps define the size and shape of the contact zone.

These elements collectively determine the distribution of contact pressure. Additionally, wheel and rail profiles vary according to the history of railway development and standardized requirements. In France, standard NF F01-115 defines the dimensional characteristics of running surfaces for rolling stock that operates on a standard gauge (about the standard wheel profile). For rails, standard NF A 45-317 defines the characteristics of the 60 kg/m Vignole rail (related to the UIC 60 rail). These standards ensure interoperability, performance, and safety on the French rail network.

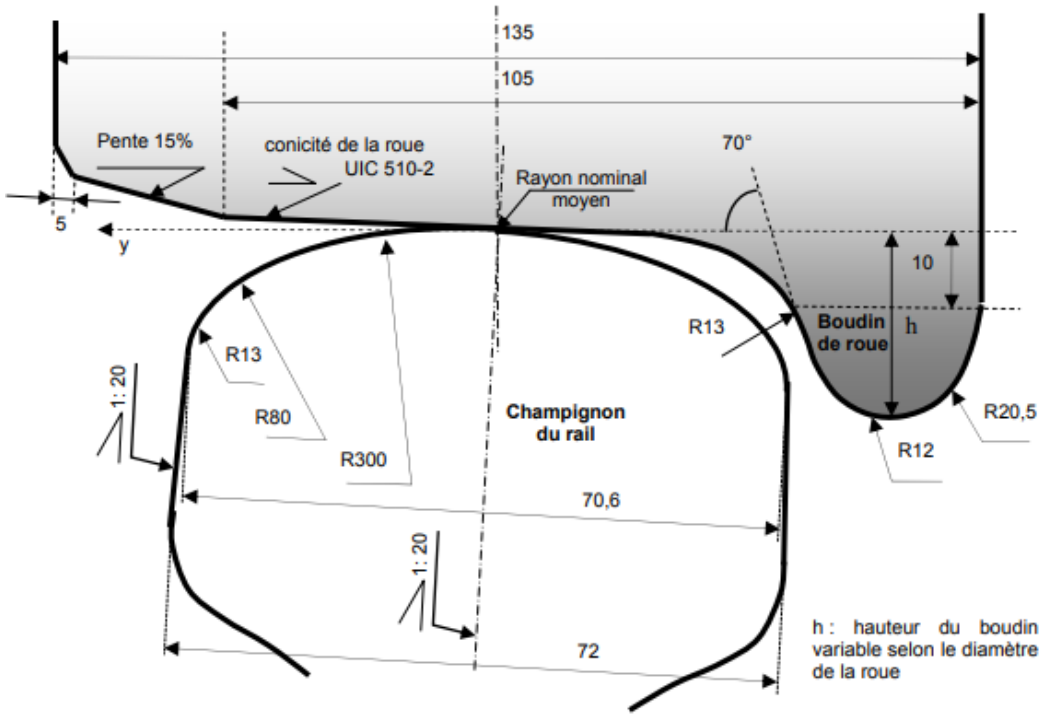

Figure 6: Rail head and wheel tread profiles [14].

The analysis of wheel and rail profiles is based on several key aspects:

- Wear and elastic deformation: Over time, wear occurs due to the continuous interaction between the wheel and rail, gradually changing the geometric characteristics of the profiles. Additionally, elastic deformation results from the applied loads and is reversible to some extent. Although figure 6 shows ideal profiles (without wear or deformation), accurate modeling must incorporate wear patterns and elastoplastic behavior to truly reflect the actual changes in dimensions and shapes.

- Vehicle stabilization and guidance: The wheel flange plays a crucial role in limiting the lateral displacement of the axle (along the y axis) by guiding the wheel and preventing excessive deflection from contact with the rail head. This interaction ensures optimal wheel alignment, which contributes to vehicle stability and reduces the risk of derailment.

- Compensating for differences in curve travel: The conicity of the tread is designed to accommodate the differences in distance traveled by the inner and outer wheels while navigating curves. y adjusting the contact radius with the rail, this feature helps to keep the axle centered and evenly distribute the load, thereby ensuring the safety and longevity of the railway system.

Although the theoretical contact between the wheel and rail is a single point, the load from the vehicle causes elastic deformation in both the wheel and rail steel. As illustrated in Table 2, this deformation extends the contact zone beyond the ideal point. This extension ensures a more even distribution of the load and enhances the stability of the railway vehicle.

	Locomotive	Heavy wagon	TGV trailer	Subway car	Tram motor unit
kg	11250	9375	8000	3750	5000
kN	110	92	78.5	36.8	49

Table 2: Typical wheel loads by type of railway vehicle [14].

According to Hertz's theory, the contact zone is analyzed in the static regime, without considering the dynamic transmission of forces. The most elementary solution is to model the contact using two cylinders with perpendicular axes. The first cylinder, representing the rail head, has its axis aligned with the direction of displacement, usually referred to as x. The second cylinder, which represents the wheel, has its axis oriented in the y direction, as shown in the figure 7. This simplification provides a reasonable approximation of the wheel-rail contact behavior within the framework of Hertz's theory.

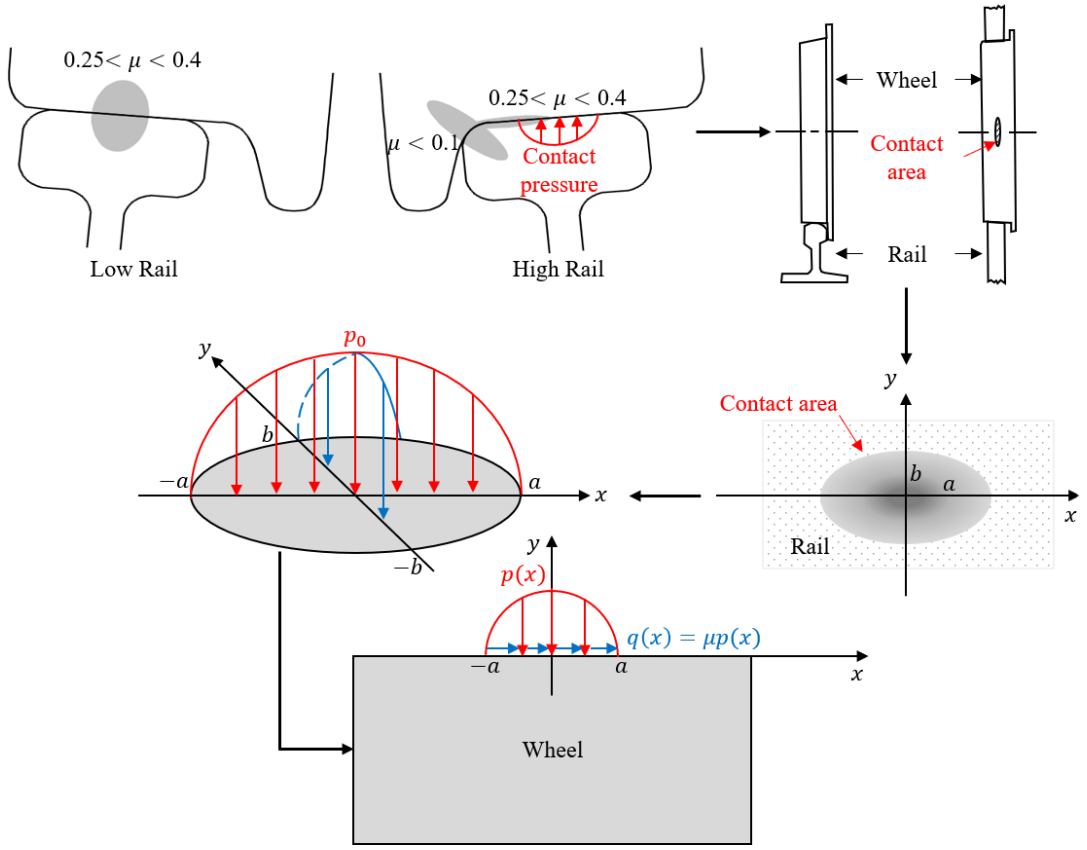

Figure 7: Hertz contact ellipse of two static cylinders.

The contact zone, calculated analytically under these conditions, forms a plane ellipse. The half-axes a and b of the ellipse are determined using the following relations:

$$\frac{a}{m} = \frac{b}{n} = \sqrt[3]{\frac{3\pi}{2}.\frac{k_1 + k_2}{A + B}.P} \tag{26}$$

with:

- $A(m^{-1})$ is the inverse of the radius of the cylinder that models the rail head,
- $B(m^{-1})$ is the inverse of the radius of the cylinder that models the wheel,
- $k_1(N^{-1}.m^2)$ and $k_2(N^{-1}.m^2)$ are the constants that depend on the modulus of elasticity E and Poisson's ratio ν of the steel used for the wheel and rail. These constants are calculated using the following relation:

$$k_i = \frac{1 - \nu_i^2}{\pi E_i}, \tag{27}$$

- m and n are dimensionless coefficients that depend on the angle θ (in degrees) defined by :

$$\cos(\theta) = \frac{B - A}{B + A}, \quad \text{as shown in the Fig. 8.} \tag{28}$$

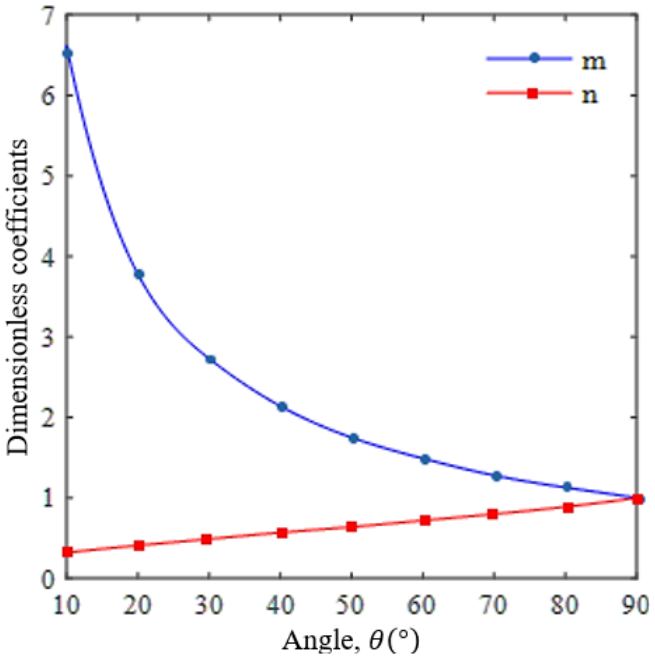

Figure 8: Evolution of the coefficients m and n as a function of θ in degrees.

These equations allow us to geometrically characterize the shape of the contact area between the wheel and the rail as a function of the material properties and dimensions of the elements in contact.

The average pressure can be calculated by dividing the force by the area of the ellipse:

$$p_{\text{average}} = \frac{P}{S} \tag{29}$$

where $P(N)$ represents the force exerted by one cylinder on another, and $S(m^2)$ denotes the area of the ellipse, calculated as:

$$S = \pi ab \tag{30}$$

The pressure at a point on the surface, as a function of the coordinates x and y of that point, is calculated as follows:

$$p(x, y) = p_0 \sqrt{1 - \left(\frac{x}{a}\right)^2 - \left(\frac{y}{b}\right)^2}, \quad \forall -a \leq x \leq a, -b \leq y \leq b \tag{31}$$

$$P = \int_{SC} p(x, y)\, ds = p_0 \int_{SC} \sqrt{1 - \frac{x^2}{a^2} - \frac{y^2}{b^2}}\, ds \tag{32}$$

où $x = a\rho\cos\theta$, $y = b\rho\sin\theta \Rightarrow ds = 2\pi ab\rho d\rho$ $(0 \leq \rho \leq 1)$

$$P = 2\pi abp_0 \int_0^1 \sqrt{1 - \rho^2}\rho d\rho \Rightarrow P = \frac{2}{3}\pi abp_0 \tag{33}$$

The maximum pressure occurs at the center of the ellipse for $x = 0$ and $y = 0$:

$$p_0 = \frac{3P}{2\pi ab} = \frac{3}{2}\frac{P}{S} = \frac{3}{2}p_{\text{average}} \tag{34}$$

The contact force per unit length is given by :

$$F = \frac{\pi b}{2}p_0 = \frac{3P}{4a} \tag{35}$$

The table 3 presents the maximum contact pressure p_0 and the half-length of the contact zone a for elliptical wheel-rail contact.

P (kN)	F (MN/m)	p_0 (MPa)	a (mm)	b (mm)	S (cm^2)
23.2	4	764.5	4.4	3.3	0.5
53.7	7	1011.4	5.8	4.4	0.8
120.6	12	1324.2	7.5	5.8	1.4
221.5	18	1621.8	9.2	7.1	2.1
299.3	22	1793.0	10.2	7.8	2.5

Table 3: Elliptical wheel-rail contact conditions define the geometry and the loads applied to the elliptical contact zone between the wheel and the rail.

5.2 Airy Function

In the context of plane elasticity, we consider a solid S treated as a semi-infinite space subjected to contact forces P and Q. This analysis is conducted on a median plane of the solid, as shown in figure 9. Depending on the thickness of the solid, the state can be characterized by either plane deformations or plane stresses. In Figure 9(b), we assume that the state is characterized by plane deformations.

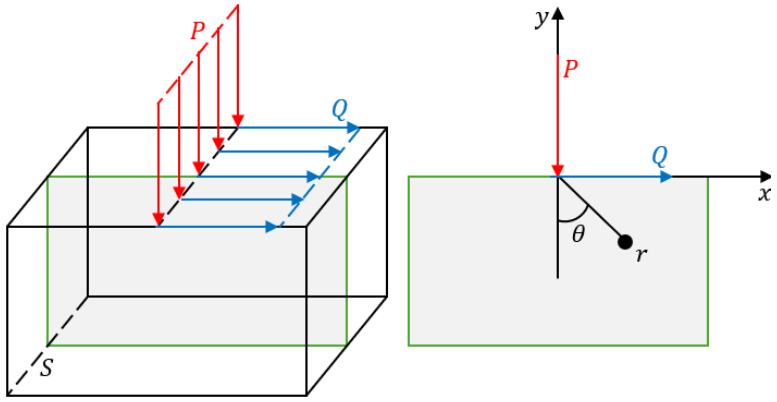

(a) 3D configuration (b) 2D configuration

Figure 9: Solid subjected to point contact forces.

Airy's function, denoted as $A(x, y)$, simplifies the analysis of stress fields in complex configurations, particularly in contact problems. Hertz's contact theory, developed by Heinrich Hertz in 1881, provides an analytical solution for describing the elastic behavior of contact between two curved bodies. It allows us to determine the distribution of stress and strain in the contact zone, depending on the elastic properties of the materials and the geometry of the bodies involved [4].

The Airy function and Hertz theory are crucial tools for analyzing contact problems in solid mechanics. The Airy function simplifies the resolution of equilibrium equations in plane elasticity, while Hertz's theory provides an analytical framework for describing behavior at contact surfaces. This is crucial for modeling stress and strain fields in various industrial applications. The combination of these

two approaches is particularly relevant for contact analyses, such as wheel-rail interactions. However, establishing a direct link between stress fields and damage mechanisms, such as wear or crack propagation, remains complex and is influenced by numerous factors.

In-plane elasticity, the railway wheel section is assimilated to a semi-infinite space, where stresses and strains are assumed to be constant in the plane and zero in the normal direction. This assumption is valid when the thickness of the section is negligible compared to its other dimensions, which is often the case for a railway wheel. Let's assume the state of plane deformations. Figure 9(b) illustrates this case, where only one dimension is considered significant compared to the other. This simplified approach transforms a three-dimensional problem into a two-dimensional one, making it easier to analyze and model the mechanical behavior of the railway wheel.

In fact, it is a linear elasticity problem in which an elastic half-space bounded by the plane surface $z = 0$ is subjected to normal and tangential loads applied to a restricted zone S of its surface. Outside this zone, the loads are zero. Because of this restriction, the stress components in this half-space can be expressed in terms of normal pressure $p(x, y)$ and tangential forces $q(x, y)$, which generally vary in the x and y directions. This type of problem is commonly encountered in the analysis of structures subjected to localized loads.

The problem of plane elasticity in a half-space subjected to loads was solved by Flamant in 1892. The Airy function $A(r, \theta)$, used to describe stresses in this case, is defined as follows:

$$A(r, \theta) = Br\theta \sin\theta + Cr\theta \cos\theta \tag{36}$$

The stresses are given by :

$$\begin{aligned} \sigma_r &= \frac{1}{r}\frac{\partial A}{\partial r} + \frac{1}{r^2}\frac{\partial^2 A}{\partial \theta^2} = \frac{2B}{r}\cos\theta - \frac{2C}{r}\sin\theta \\ \sigma_\theta &= \sigma_{r\theta} = 0 \end{aligned} \tag{37}$$

The constants B and C are determined by equilibrating the contact forces P and Q with the stresses acting on a semi-circle of radius r :

$$\begin{aligned} -P &= \int_{-\frac{\pi}{2}}^{\frac{\pi}{2}} \sigma_r \cos\theta r d\theta = B\pi \Rightarrow B = -\frac{P}{\pi} \\ -Q &= \int_{-\frac{\pi}{2}}^{\frac{\pi}{2}} \sigma_r \sin\theta r d\theta = C\pi \Rightarrow C = -\frac{Q}{\pi} \end{aligned} \tag{38}$$

Therefore, the stress function $A(r, \theta)$ and the stress σ_r can be written as :

$$\begin{aligned} A(r, \theta) &= -\frac{r\theta}{\pi}(P\sin\theta + Q\cos\theta) \\ \sigma_r &= -\frac{2}{\pi r}(P\cos\theta - Q\sin\theta) \end{aligned} \tag{39}$$

where P is the applied normal load, Q is the applied tangential load, r is the radial distance from the load point, and θ is the polar angle with respect to the x axis. This Airy function is a solution of the biharmonic equation in an elastic half-space. It is used to determine the stresses induced by the loads applied to the surface of the half-space.

The stresses in Cartesian coordinates as a function of σ_r are given by :

$$\begin{aligned}\sigma_{xx} &= \sigma_r \sin^2\theta \\ \sigma_{yy} &= \sigma_r \cos^2\theta \\ \tau_{xy} &= \sigma_r \sin\theta\cos\theta\end{aligned} \tag{40}$$

where $\cos\theta = -\frac{y}{r}$ et $\sin\theta = \frac{x}{r}$, σ_x, σ_y, τ_{xy} are expressed as :

$$\begin{aligned}\sigma_{xx} &= \frac{2}{\pi}\frac{Px^2y + Qx^3}{(x^2+y^2)^2} \\ \sigma_{yy} &= \frac{2}{\pi}\frac{Py^3 + Qxy^2}{(x^2+y^2)^2} \\ \tau_{xy} &= -\frac{2}{\pi}\frac{Pxy^2 + Qx^2y}{(x^2+y^2)^2}\end{aligned} \tag{41}$$

Now let's consider arbitrary contact pressures $p(s)$ and $q(s)$, distributed over a length $2a$ of the half-plane (Figure 10).

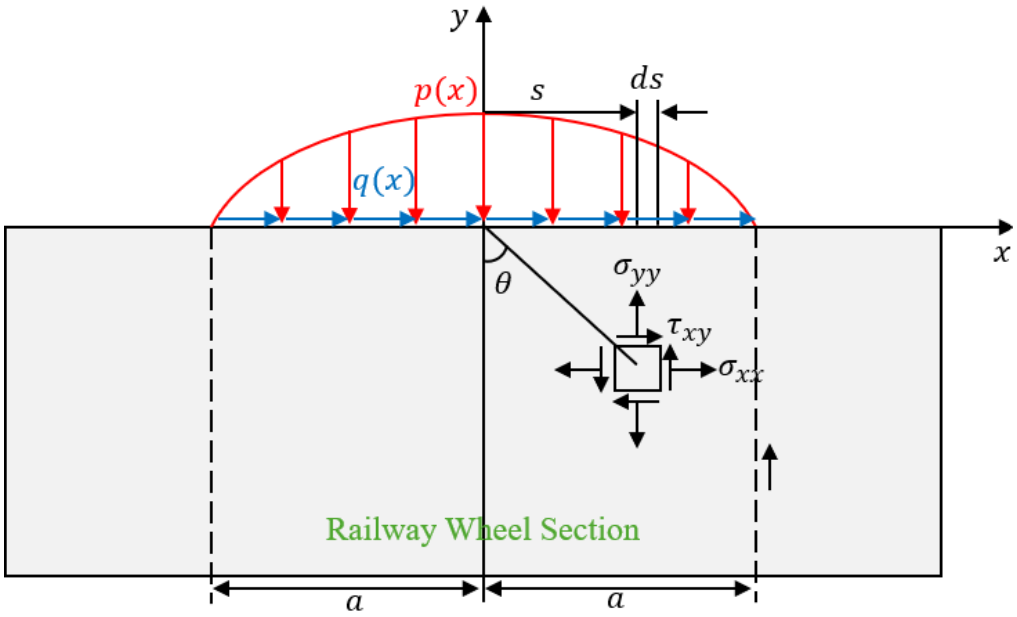

Figure 10: Railway wheel section subjected to normal $p(x)$ and tangential $q(x)$ loads.

By replacing P by $p(s)ds$, Q by $q(s)ds$, and x by $x - s$ to take into account the reference frame translation, the stresses given by the previous equations become :

$$\begin{aligned}\sigma_{xx}(x,y) &= \frac{2y}{\pi}\int_{-a}^{a}\frac{p(s)(x-s)^2}{[(x-s)^2+y^2]^2}ds + \frac{2}{\pi}\int_{-a}^{a}\frac{q(s)(x-s)^3}{[(x-s)^2+y^2]^2}ds \\ \sigma_{yy}(x,y) &= \frac{2y^3}{\pi}\int_{-a}^{a}\frac{p(s)}{[(x-s)^2+y^2]^2}ds + \frac{2y^2}{\pi}\int_{-a}^{a}\frac{q(s)(x-s)}{[(x-s)^2+y^2]^2}ds \\ \tau_{xy}(x,y) &= -\frac{2y^2}{\pi}\int_{-a}^{a}\frac{p(s)(x-s)}{[(x-s)^2+y^2]^2}ds - \frac{2y}{\pi}\int_{-a}^{a}\frac{q(s)(x-s)^2}{[(x-s)^2+y^2]^2}ds\end{aligned} \tag{42}$$

with:

$$p(s) = p_0\sqrt{1 - \frac{s^2}{a^2}} \tag{43}$$

and,

$$q(s) = \mu p(s) \tag{44}$$

The integrals of equations (42) were programmed using Matlab. Numerical simulations were carried out to study stresses in the case of an elliptical wheel-rail contact, taking into account friction at the wheel-rail interface. The representation of stresses as a function of the abscissa x scaled by the maximum contact pressure p_0 and the half-length of the contact zone a is one approach used to visualize the evolution of stresses along the contact surface. The variation in stresses σ_{xx} and τ_{xy} that can be observed with the presence of friction is as expected. Friction introduces local stress variations due to the additional tangential forces generated by friction between wheel and rail. This can lead to stress peaks, particularly in the tangential direction τ_{xy}, which has an impact on the maximum shear stress $\tau_{\max}$. This analysis is useful for understanding how friction affects stresses in the wheel-rail contact, which may have important implications for the design and durability of the railway wheel.

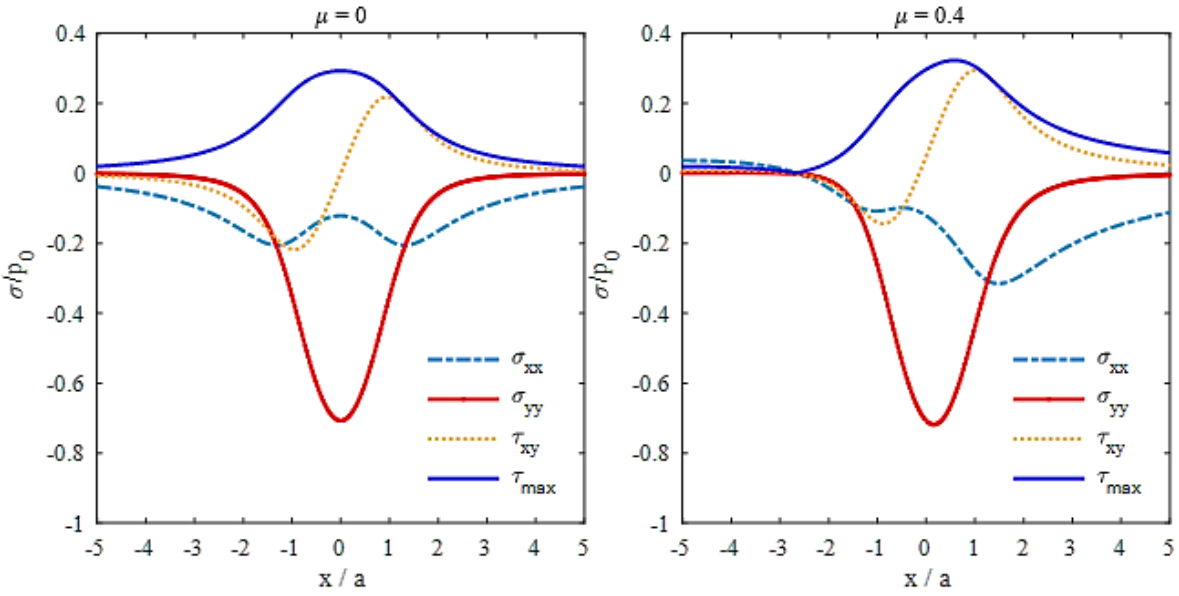

Figure 11: Evolution of stresses σ/p_0 as a function of x/a in a defect-free wheel section in the case of elliptical wheel-rail contact without friction ($\mu = 0$) on the left and with friction ($\mu = 0$) on the right: $P = 80$ kN.

Figure 11 illustrates the evolution of stresses σ/p_0 as a function of x/a in a defect-free wheel section, subjected to a load $P = 80\,\text{kN}$ in the case of an elliptical wheel-rail contact. The equations (42) describing normal and tangential stresses in the $x - y$ plane of the elastic half-space have been used to represent these stresses. These stresses are normalized by the maximum contact pressure p_0 and, consequently, these stresses can be plotted as a function of the dimensionless position x/a in the contact zone. In this case, the following assumptions were used:

- $R_{\text{wheel}} = 0.445$ m,
- $R_{\text{rail}} = 0.3$ m,
- $\nu = 0.3$,
- $E = 210$ GPa,

- $h = a = 6.6$ mm where h is the depth of the element,
- $L = 0.2$ m where L represents the length of the railway wheel section.

These stresses are also y position-dependent, so to plot the evolution of stresses along the contact zone, it is necessary to select specific values of y for each data point.

The equations of stress (42) cannot generally be integrated analytically, requiring the use of numerical methods such as the finite element method (FEM). The FEM is particularly well suited to modeling complex structures and solving elasticity problems under realistic conditions, such as wheel-rail contact. The method enables the wheel-rail contact zone to be accurately modeled and the stresses in this zone to be calculated numerically, taking into account the geometry, material properties of the railway wheel, loading conditions, and boundary conditions. The comparison of results obtained from Hertz contact theory with those obtained from finite element analysis is a valid approach for validating and verifying the accuracy of numerical models. This ensures that the numerical models correctly reproduce the expected behavior of the railway wheel. Figure 12 shows the time evolution of normal and shear stresses during a loading cycle. It can be seen that the numerical model has been successfully validated by comparing theoretical results with those obtained numerically.

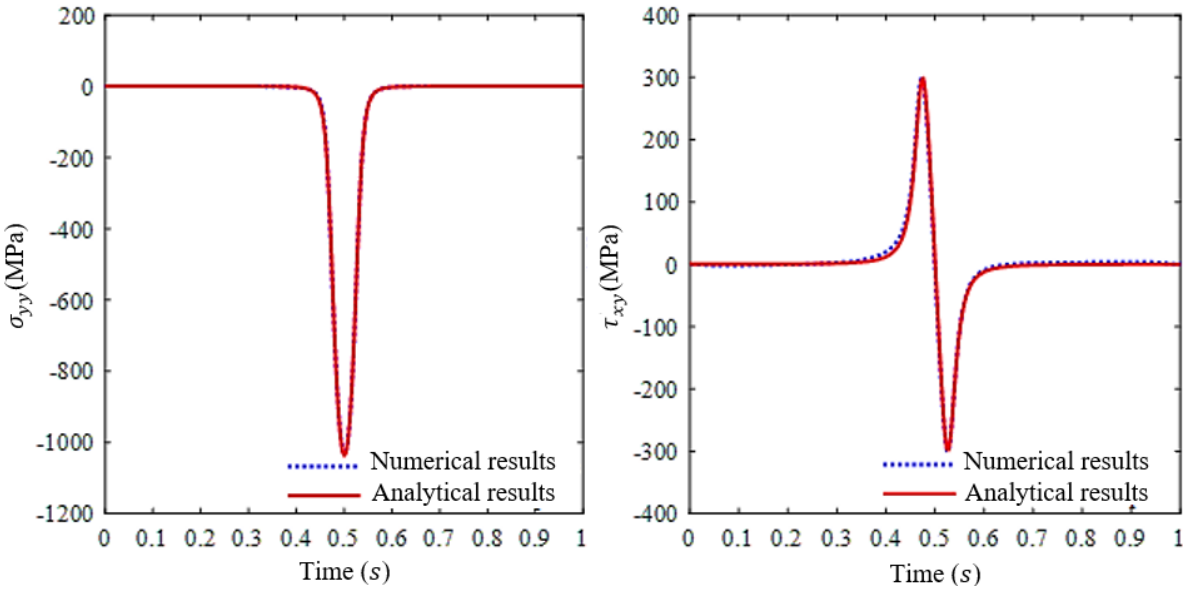

Figure 12: Evolution of normal stress σ_{yy} and shear stress τ_{xy} during a load cycle in a defect-free wheel section, subjected to a load $F = 12$ MN/m, neglecting friction at the wheel-rail interface in the case of linear wheel-rail contact.

By neglecting friction, the results obtained can be used as a basis for comparing the behavior of the rail wheel cross-section with and without friction. This makes it possible to evaluate the effect of friction on the stresses and strains of the rail wheel. Indeed, the relationship (42) gives the results in terms of stresses when friction at the wheel-rail interface is neglected.

Figure 13 shows the isostresses of maximum shear stress $\tau_{\max}$ as a function of abscissas x and y scaled by maximum contact pressure p_0 and contact half-length a in a section of a defect-free railway wheel for F = 12 MN/m without friction in the case of linear wheel-rail contact. It can be seen that τ_{max} is maximal at a depth $h = 0.78\ a$ from the contact surface and is of the order of $0.3\ p_0$.

The expression for the strain ε_{zz} in elasticity is given by :

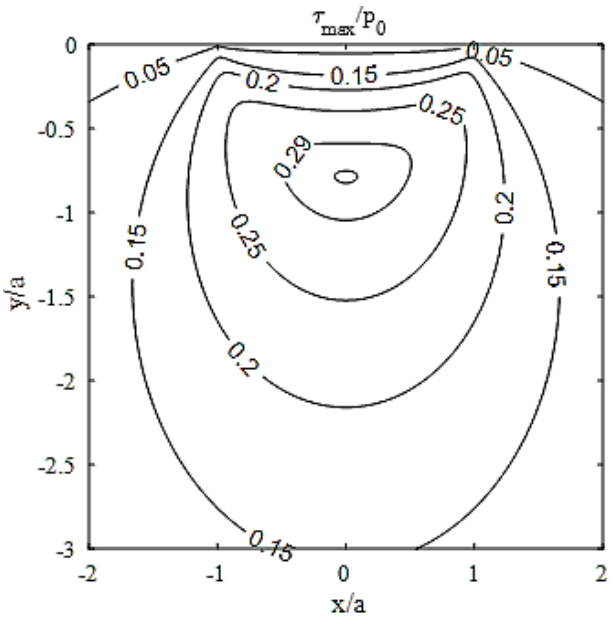

Figure 13: Isostresses τ_{max}/p_0 as a function of x/a and y/a obtained theoretically with Matlab in a defect-free railway wheel section subjected to a load F = 12 MN/m in the case of linear wheel-rail contact.

$$\varepsilon_{zz} = \frac{1}{E}\left[\sigma_{zz} - \nu\left(\sigma_{xx} + \sigma_{yy}\right)\right] \tag{45}$$

For the assumption of the plane strain state where $\varepsilon_{zz} = 0$, the expression of the normal stress in lateral direction σ_{zz} is always given by :

$$\sigma_{zz} = \nu\left(\sigma_{xx} + \sigma_{yy}\right) \tag{46}$$

The expression of the equivalent Von Mises stress is given by the following equation:

$$\sigma_{\mathrm{eq,VM}} = \sqrt{\frac{(\sigma_{xx} - \sigma_{yy})^2 + (\sigma_{yy} - \sigma_{zz})^2 + (\sigma_{zz} - \sigma_{xx})^2 + 6\tau_{xy}^2}{2}} \tag{47}$$

The isostresses in Figure 14 show how equivalent Von Mises stress $\sigma_{\mathrm{eq,\ VM}}$, shear stress τ_{xy}, and normal stress σ_{yy} vary across a railway wheel—in a defect-free section. Those stresses are normalized by the maximum contact pressure and the wheel's contact half-length. For a 12 MN/m load with no friction and linear wheel-rail contact, it can be seen that shear stress peaks at about half that length, $h = 0.5$ a, and is roughly 0.25 times the maximum contact pressure (0.25 p_0). Normal stress is at its highest at the point of contact ($h = 0$) where that pressure is at its maximum. Both of those maxima are right in the middle of the stress distributions.

Depths $h = 0$ and 0.5 a were used to determine a railway wheel's stress state. The depth $h = 0.78$ a was used to locate a geometric defect in the wheel material. The Von Mises equivalent stress pattern obtained theoretically is qualitatively similar to that obtained numerically. However, the difference between theoretical and numerical results remains significant, of the order of 15.3 %.

The analytical and numerical isostresses matched well. However, it is important to understand that these theoretical results depend on Hertz's contact theory, which assumes purely elastic behavior of materials in contact. This theory predicts the shape and size of the contact area, and the stress distribution, all based on the elasticity of the materials. To understand how materials behave beyond

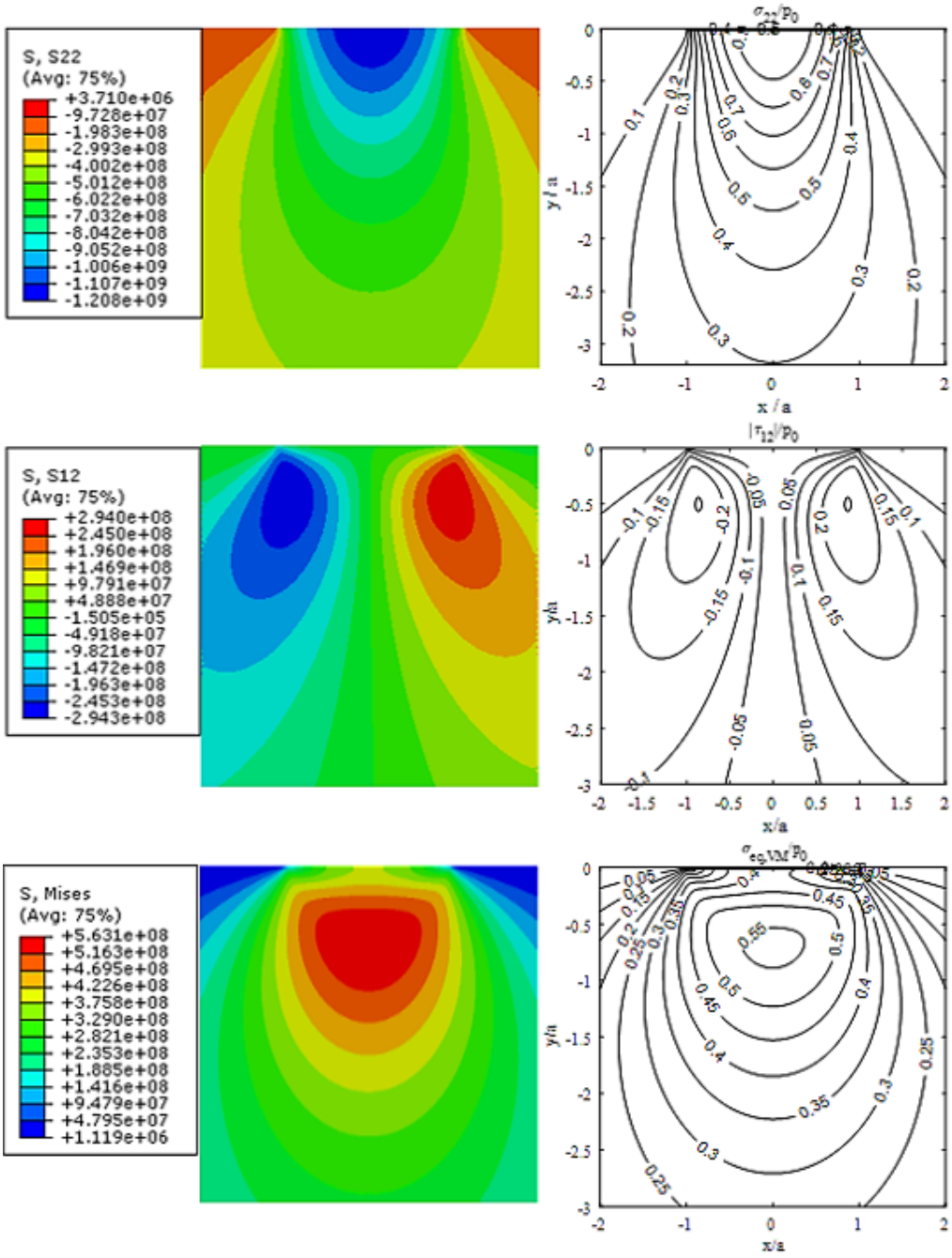

Figure 14: Isostresses $\sigma_{\mathrm{eq,VM}}/p_0$, $|\tau_{12}|/p_0$ and σ_{22}/p_0 as a function of x/a and y/a obtained numerically (left) and analytically (right) in a defect-free railway wheel section subjected to a load $F = 12$ MN/m in the case of a linear wheel-rail contact.

elasticity, the finite element method has been used. This method models nonlinear behavior, such as elastoplasticity, considering the material's properties and loading conditions.

5.3 Numerical stress and strain analysis

The railway wheel experiences significant stress from the train's weight, speed, and braking force on the wheel. The heat increases because of friction between the brake pad and the wheel surface, leading to high residual tensile stress. However, our numerical model did not consider temperature effects. To study the wheel's stress, we refined the mesh near the contact zone, where stress and strain gradients are significant, as shown in Figure 15.

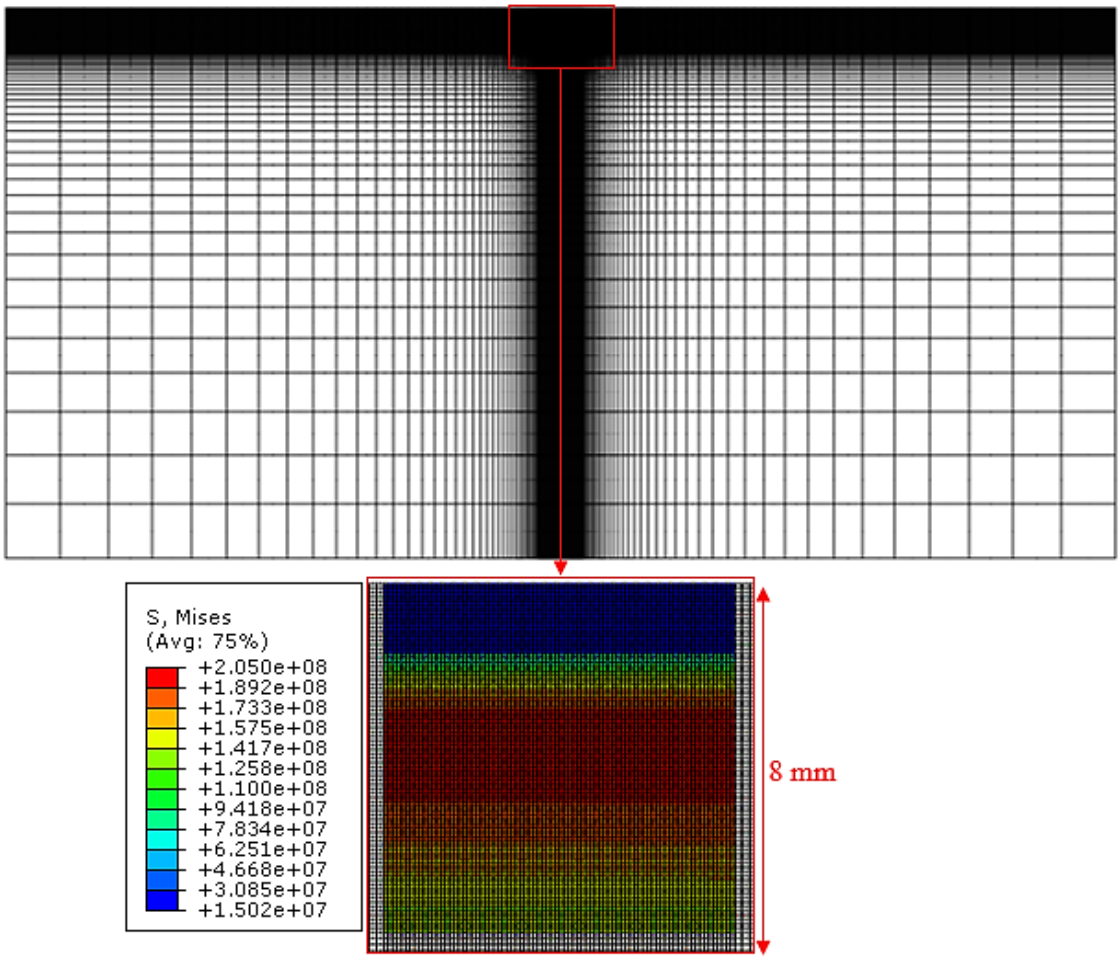

Figure 15: Mesh refinement near the contact zone of a defect-free railway wheel section subjected to $F = 12$ MN/m without friction in the case of linear wheel-rail contact.

6 Loading influence

Static analysis was performed to investigate the stress evolutions along loading cycles when a train wheel rolls on a rail. This phenomenon generates a multiaxial and non-proportional state of stress, for which an effective fatigue criterion is needed. The first assumption is that the wheel-rail contact surface is ideally smooth. However, in reality, these surfaces have some irregularities, like roughness and indentations, that affect the distribution of stress. This leads to a notable difference from the predictions made by Hertz's contact theory.

In this analysis, the zone in which the equivalent Von Mises stress is maximum was used as the critical zone of the model to determine wheel life. The other quantities studied were the equivalent plastic strain and the maximum fatigue parameter. It was found that the maximum value of these quantities is located in the critical zone of the wheel section, but not necessarily in the same mesh

element. Consequently, the best way to save computation time when quantifying RCF damage is first to identify the critical zone where the maximum value of the equivalent Von Mises stress is located, during the last loading cycle, and where crack initiation is expected. Crack initiation occurs at different depths, depending on the loading level and the coefficient of friction.

The axle load values studied are: $F = 7$, 12, 18, and 22 MN/m. They correspond respectively to maximum contact pressures $p_0 = 922.75$, 1208.2, 1479.7, and 1635.9 MPa.

6.1 Stresses and strains

Figure 16 shows the evolution of Von Mises stress and cumulative equivalent plastic strain (PEEQ) as a function of axle load, without friction in the case of a linear wheel-rail contact. The Von Mises equivalent stress peaks during the last loading cycle, and the equivalent plastic strain (PEEQ) peaks after the load has passed. It can be seen that, for $F = 7$ MN/m, the material does not yield, as the Von Mises equivalent stress obtained is of the order of 533.6 MPa and below the yield strength of the order of 543 MPa, so the equivalent plastic strain is zero. For $F = 12$ MN/m, the Von Mises equivalent stress is of the order of 543.8 MPa, so the material yields slightly (equivalent plastic deformation of the order of 0.2 %). In this case, it can be said that the material is just beginning to yield. For $F = 18$ and 22 MN/m, the Von Mises equivalent stress is well above the yield strength, so there is clear plasticity in the material. What's more, both the Von Mises equivalent stress and the equivalent plastic deformation increase with increasing axle load.

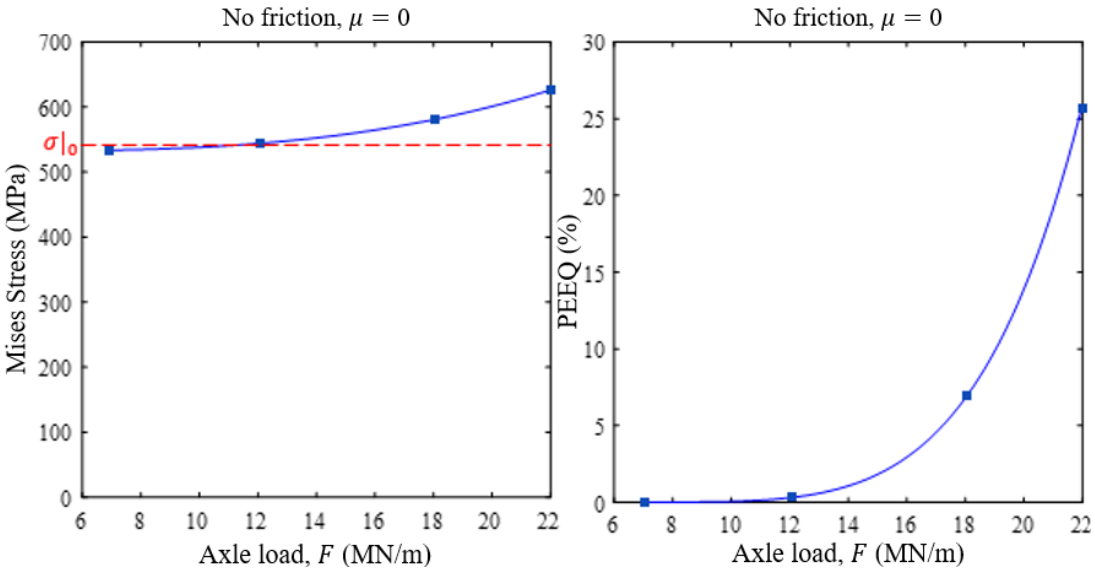

Figure 16: Evolution of Von Mises equivalent stress and plastic strain as a function of frictionless axle load in the case of linear wheel-rail contact.

Figure 17 illustrates the Von Mises equivalent residual stress variation for various axle load levels. It is observed that the region of the maximum Von Mises equivalent stress moves toward the contact surface as the axle load increases. In fact, for an axle load of $F = 7$ MN/m, the region of the maximum Von Mises equivalent stress is not discernible due to the insufficient axle load. For $F = 12$ MPa, it is 2.6 to 5.85 mm deep from the contact surface. For $F = 18$ MN/m, it is 0.75 to 8 mm deep, and for $F = 22$ MN/m, it is 0.2 to 8 mm deep. This means that the axle load increase is synonymous with enlarging the area over which the Von Mises equivalent stress assumes its maximum value. To be more precise, the area is approximately 3.25 mm for $F = 12$ MN/m, 7.25 mm for $F = 18$ MN/m, and 7.8 mm for $F = 22$ MN/m.

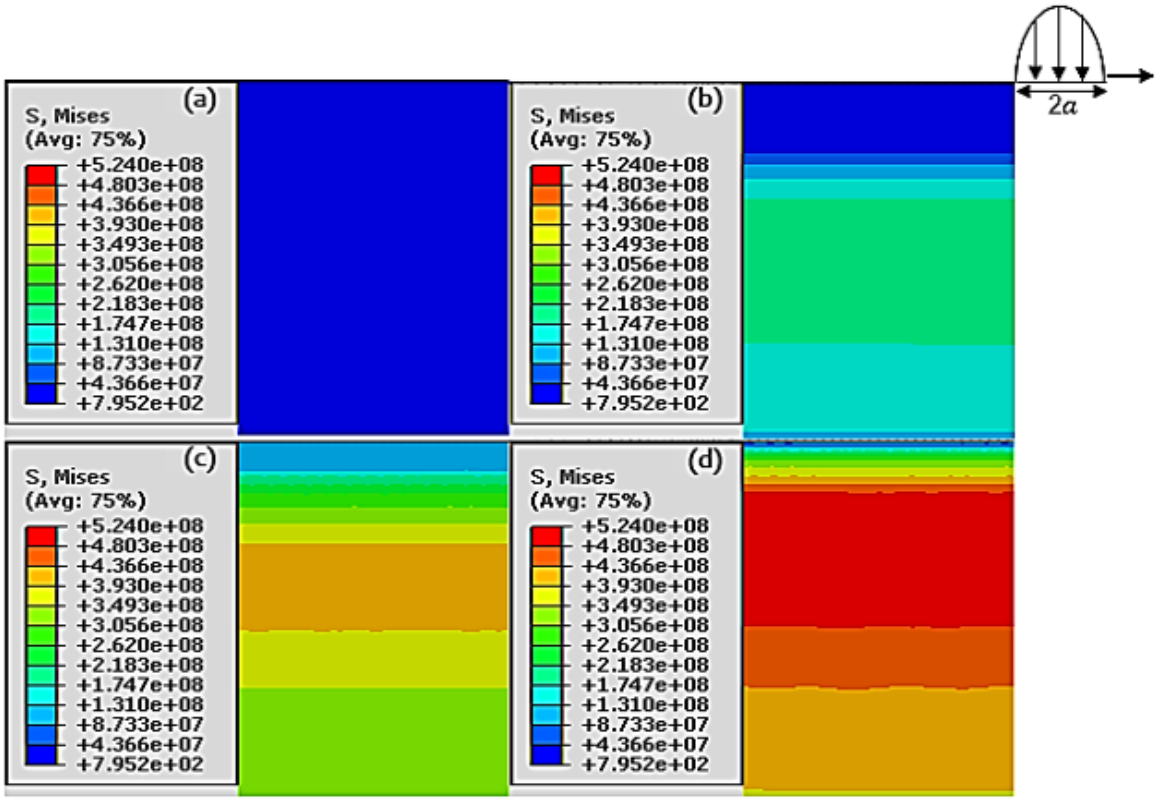

Figure 17: Von Mises equivalent residual stress distribution for: (a) $F = 7$ MN/m, (b) $F = 12$ MN/m, (c) $F = 18$ MN/m, and (d) $F = 22$ MN/m.

Figure 18 presents the residual stress distributions σ_{11}, σ_{22} and τ_{12} for F = 12 MN/m without friction in the case of a linear wheel-rail contact. It can be observed that the stress σ_{11} plays a significant role in the calculation of the Von Mises equivalent stress.

Figure 19 illustrates the distribution of the equivalent plastic deformation for different levels of axle load, measured after the last load passage. It can be observed that the region of maximum equivalent plastic strain moves towards the contact surface as the axle load increases, as it also was found for the Von Mises equivalent stress. Indeed, for $F = 7$ MN/m, the material does not plasticize. The residual equivalent plastic strain (PEEQ) is of the order of 0.2, 6.8, and 25.9 % for $F = 12$, 18, and 22 MN/m respectively. Consequently, equivalent plastic deformation increases with increasing axle load. Residual stress distributions σ_{11}, σ_{22} and τ_{12} for $F = 12$ MN/m with no friction in the case of linear wheel-rail contact.

Successive passages of a wheel on a rail can change the state and mechanical properties of the material, producing a gradient of equivalent plastic deformation in the wheel section. The location of the equivalent plastic deformation is of great importance, as RCF damage occurs in this area. This region is located at a depth of 1.7, 0.9, and 0.2 mm from the contact surface for $F = 12$, 18, and 22 MN/m respectively, as illustrated in Figure 20.

Figure 21 illustrates the residual strain distributions ε_{11}, ϵ_{22} and γ_{12} for F = 12 MN/m with no friction in the case of a linear wheel-rail contact. Notice that the γ_{12} strain has an important contribution to the determination of the equivalent plastic strain.

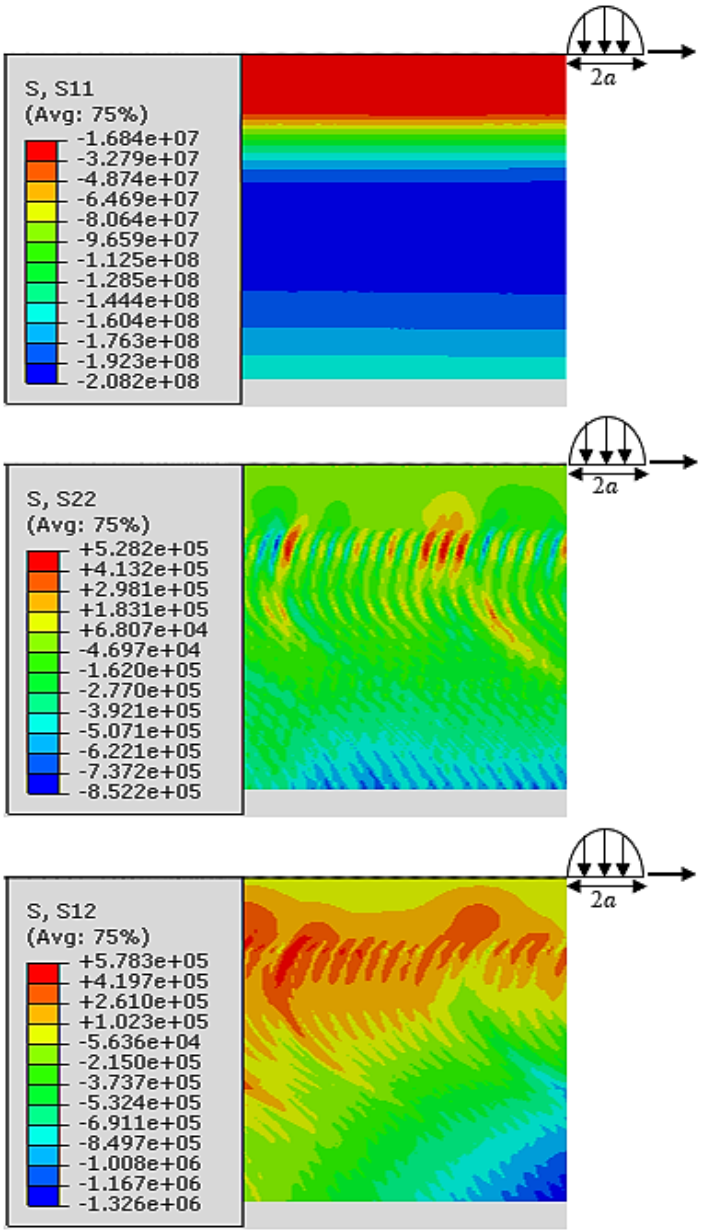

Figure 18: Residual stress distributions σ_{11}, σ_{22} and τ_{12} for $F = 12$ MN/m with no friction in the case of linear wheel-rail contact.

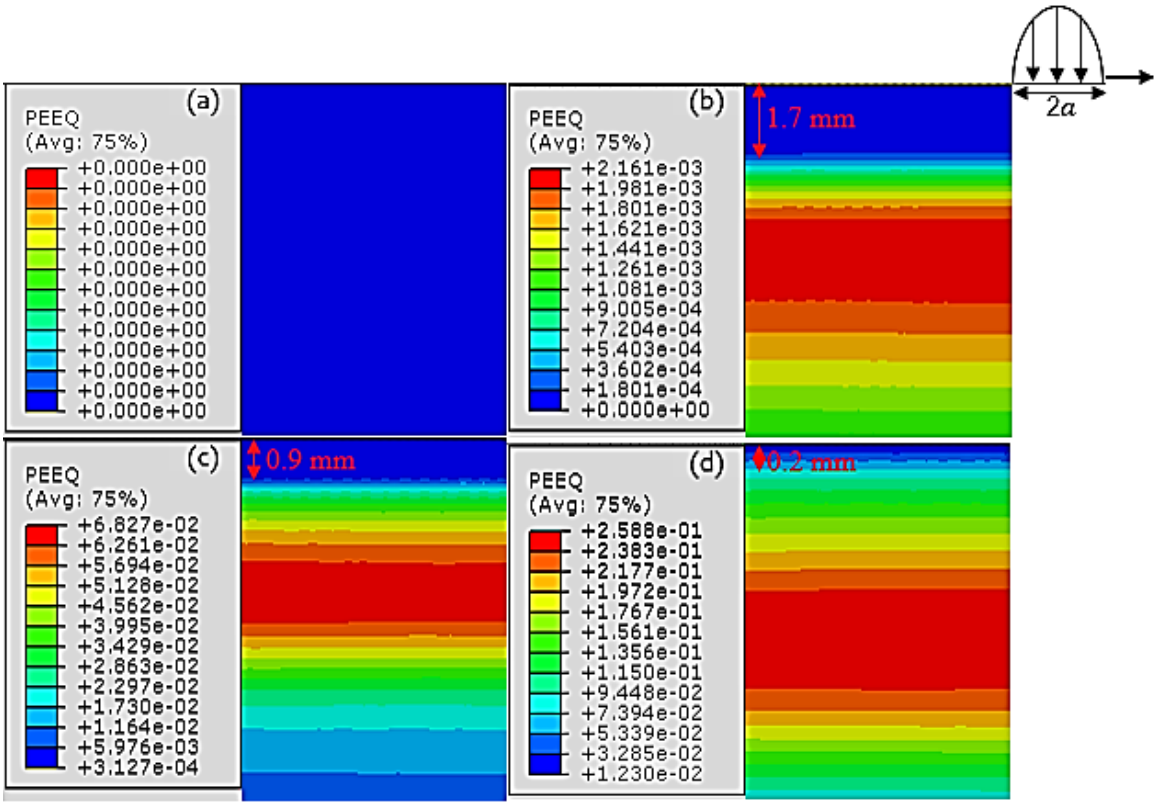

Figure 19: Distribution of equivalent plastic strain for: (a) $F = 7$ MN/m, (b) $F = 12$ MN/m, (c) $F = 18$ MN/m and (d) $F = 22$ MN/m.

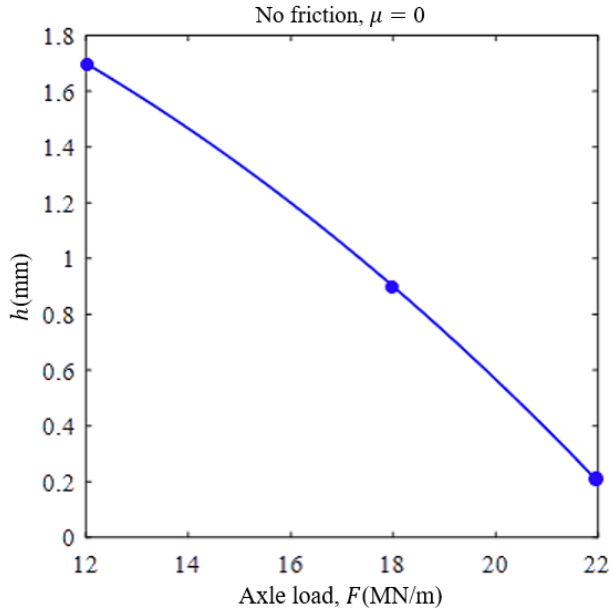

Figure 20: Depth behavior of the element that undergoes maximum value of equivalent plastic deformation as a function of axle load, with no friction in the case of linear wheel-rail contact.

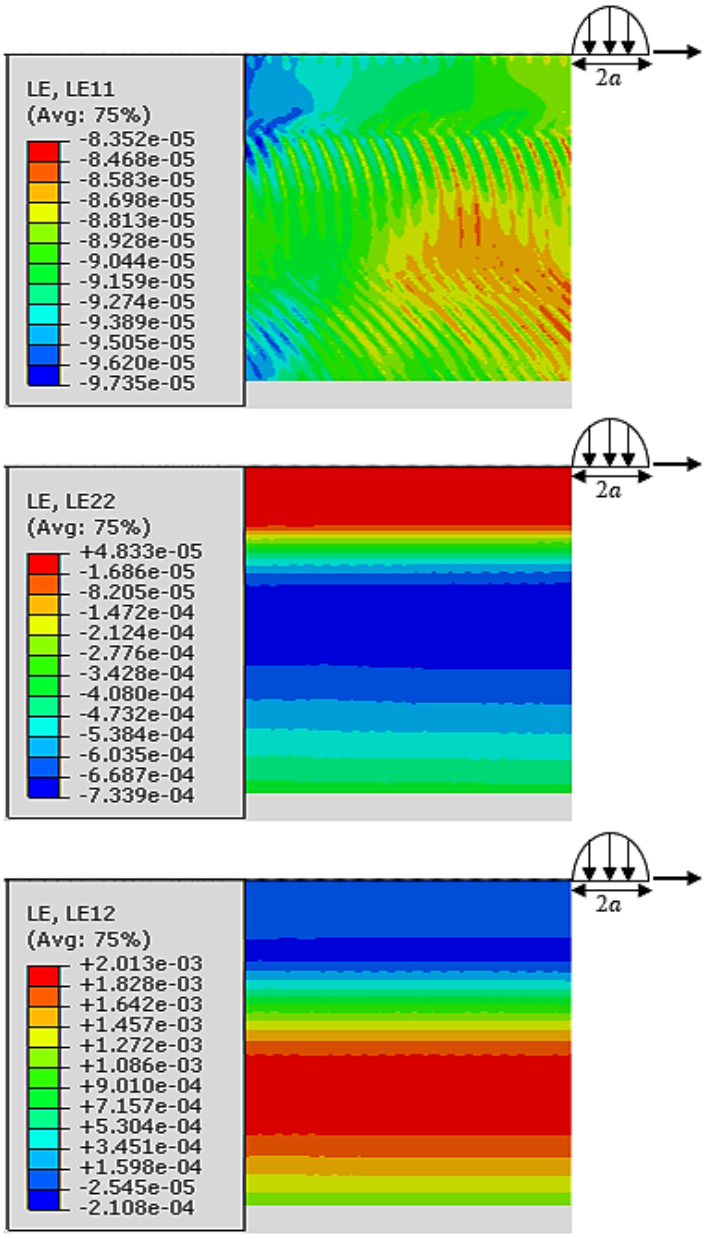

Figure 21: Residual strain distributions ε_{11}, ε_{22} and γ_{12} for $F = 12$ MN/m with no friction in the case of linear wheel-rail contact.

6.2 Damage mechanism characterization

The performance of the material under cyclic loading will reduce progressively, causing failure in either the rails or wheels. The damage can be quantified based on the stress-strain response of the wheel material. The stress and strain values chosen correspond to the response during the last loading cycle.

The distributions of normal and shear stress and strain in the middle of the last loading cycle for $F = 7$ MN/m and friction coefficient $\mu = 0$ are shown in Figure 22. The peak value of the normal compressive stress is around 922.8 MPa. This corresponds very well with the maximum contact pressure determined analytically.

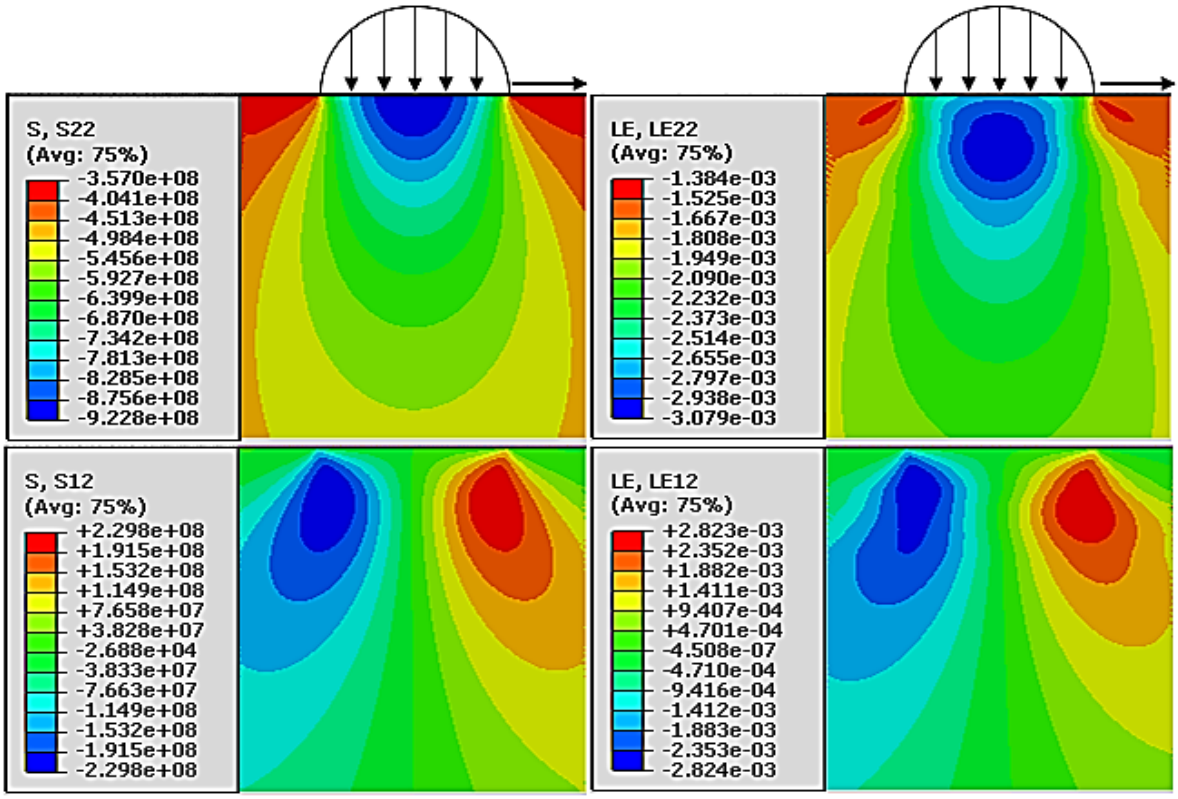

Figure 22: Normal and shear stress and strain distributions in the middle of the last loading cycle for $F = 7$ MN/m with $\mu = 0$, in the case of a linear wheel-rail contact.

Figure 23 illustrates the evolution of the normal and shear stress and strain in the most damaged element over the loading cycles. It can be observed that the maximum normal stress $\sigma_{\max}$ is around 16.3 MPa and that the variation in shear stress $\Delta\tau$ is around 461.5 MPa. This allows us to predict the mode of failure by RCF and means that the wheel damage is entirely due to shear. However, in some cases, this is not enough: one needs to also consider the values of the variation of the plastic strain amplitude in tensile-compressive $\Delta\varepsilon_p$ and the plastic strain amplitude in shear $\Delta\gamma_p$ at the crack plane.

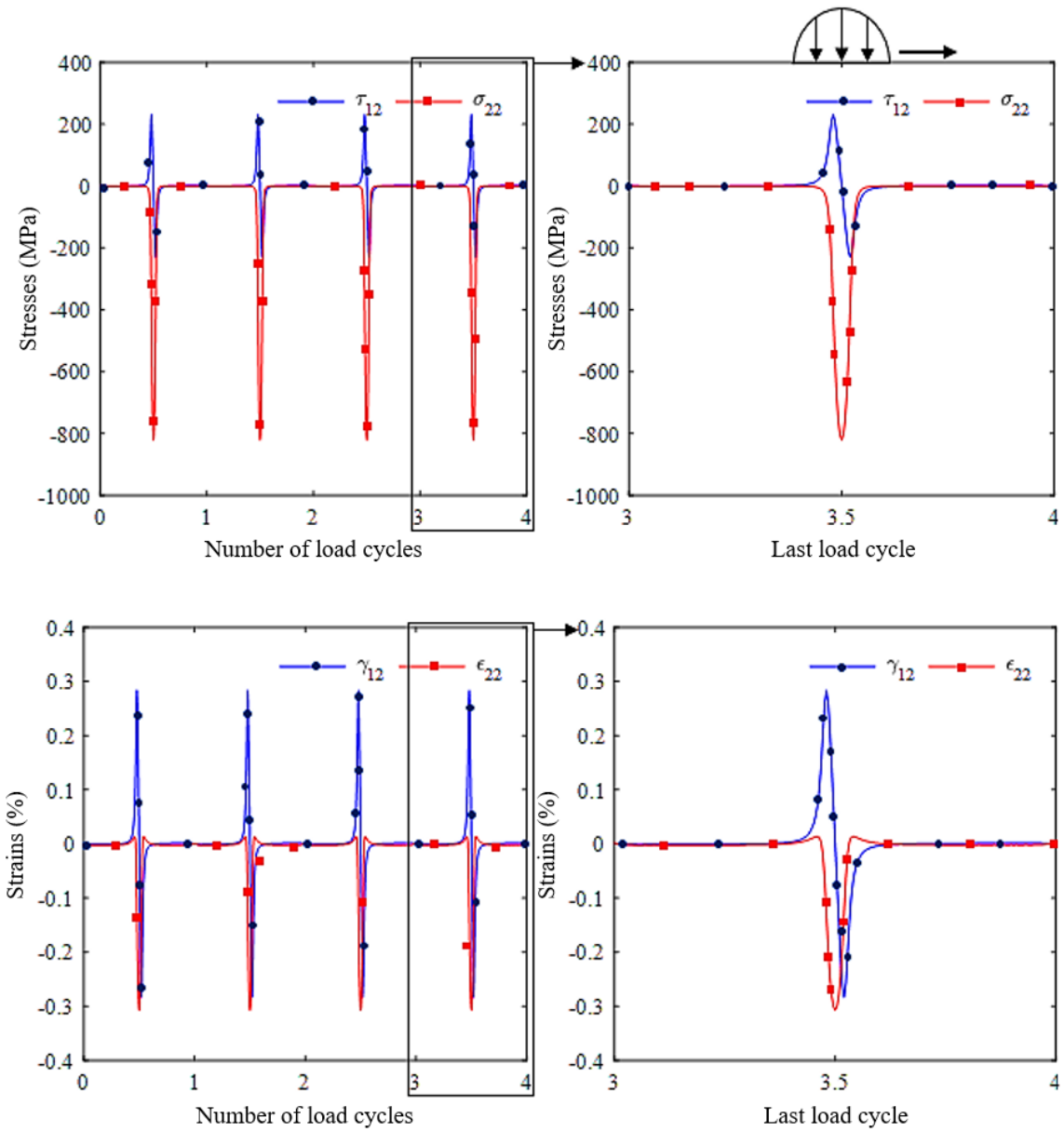

Figure 23: Evolution of stresses and strains during loading cycles for $F = 7$ MN/m with no friction in the case of a linear wheel-rail contact.

Figure 24 illustrates the evolution of normal and shear stress versus normal and shear strain respectively for $F = 7$ MN/m with $\mu = 0$, in the case of a linear wheel-rail contact. It is seen that the asymptotic behavior of the material is purely elastic. On the other hand, under real railway conditions, where plastic deformations accumulate stably (hysteresis loop) and unstably (ratchet effect), the study of plastic shakedown and ratchet phenomena is of great interest. In such conditions, the railway wheel failure occurs unexpectedly. To model these material behaviors, it is necessary to increase the level of load or friction at the wheel-rail contact. Thus, rolling and sliding conditions are assumed to exist at the wheel-rail interface, which changes the contact state and makes calculations even more complicated.

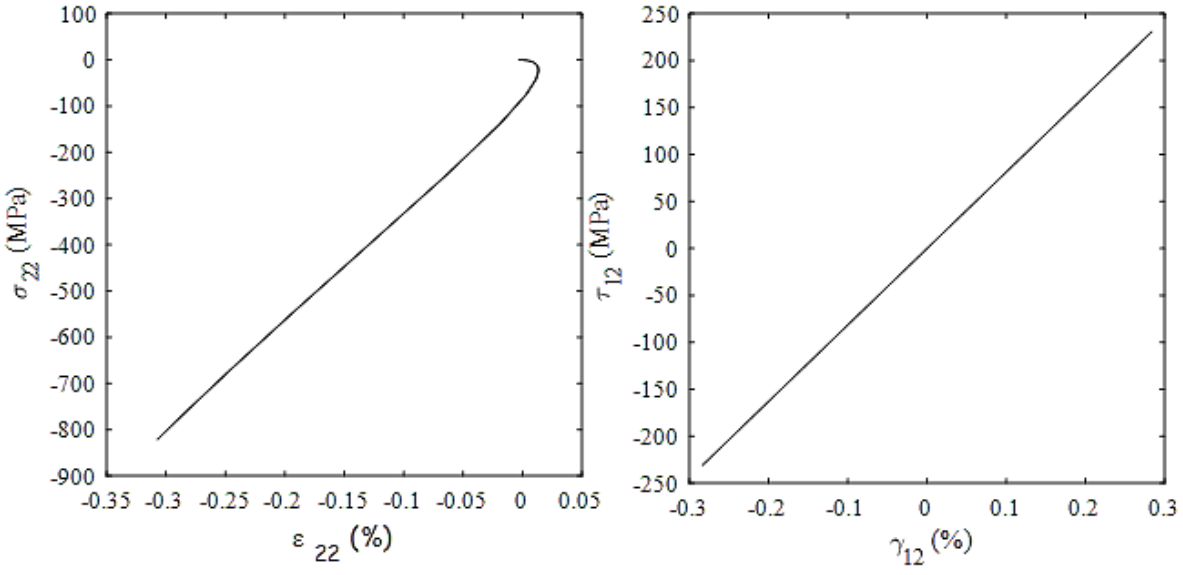

Figure 24: Évolution de la contrainte normale et de cisaillement en fonction de la déformation normale et de cisaillement pour F = 7 MN/m avec $\mu = 0$, dans le cas d'un contact roue-rail linéique.

6.3 Fatigue parameter

Damage quantification is determined from equation (1).

For $F = 7$ and 12 MN/m, with $\mu = 0$, stresses and strains that caused the fatigue damage in the linear and elliptical wheel-rail contact cases can be found in Tables 4 and 5. This data can be taken from Figure 25 for the elliptical wheel-rail contact case.

F (MN/m)	$\sigma_{\max}$ (MPa)	$\Delta\varepsilon_p$ (%)	$\Delta\tau$ (MPa)	$\Delta\gamma_p$ (%)	$\mathrm{FP}_{\max}$ (MPa)
7	14.04	0.17	404.19	0.17	0.15
12	0	0.098	598.06	0.27	0.33

Table 4: Stresses and strains on the critical plane and the maximum fatigue parameter $FP_{\max}$ for different load levels with $\mu = 0$, in the linear wheel-rail contact case.

F (MN/m)	$\sigma_{\max}$ (MPa)	$\Delta\varepsilon_p$ (%)	$\Delta\tau$ (MPa)	$\Delta\gamma_p$ (%)	$\mathrm{FP}_{\max}$ (MPa)
7	0	0.38	437.60	0.24	0.21
12	0	1.27	605.71	0.31	0.37

Table 5: Stresses and strains on the critical plane and the maximum fatigue parameter $FP_{\max}$ for different load levels with $\mu = 0$, in the elliptical wheel-rail contact case.

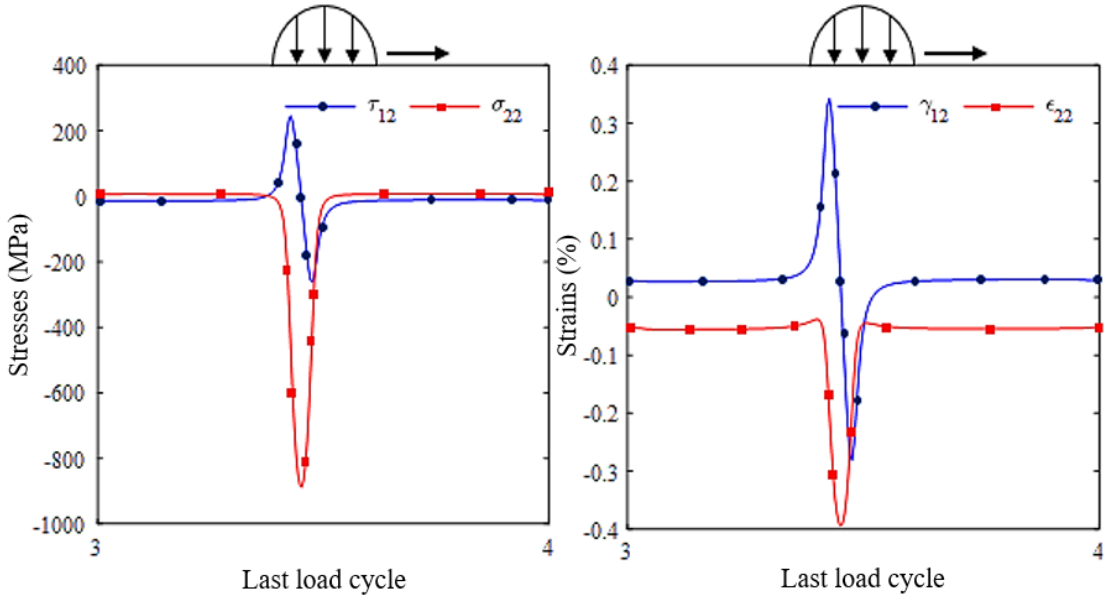

Figure 25: Evolution of normal and shear stress and strain on the crack plane during the last loading cycle for $F = 7$ MN/m in the elliptical wheel-rail contact case.

Figure 26 shows the evolution of the fatigue parameter versus the orientation angle of the material plane under the conditions of $F = 7$ MN/m and $\mu = 0$. This comparison is made for both linear and elliptical wheel-rail contact cases. The maximum fatigue parameter ($FP_{\max}$) in the linear wheel-rail contact case is approximately 0.15 MPa and corresponds to a critical plane orientation angle around 116 °. However, in the elliptical wheel-rail contact case, $FP_{\max}$ reaches a higher value of approximately 0.21 MPa, corresponding to a critical plane orientation angle near 151 °. This difference underscores the impact of contact geometry on fatigue behavior.

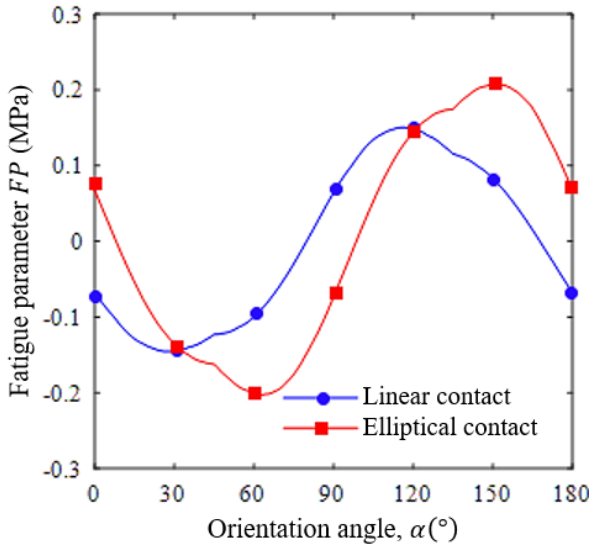

Figure 26: Evolution of the fatigue parameter versus material plane orientation angle for $F = 7$ MN/m with $\mu = 0$, in the linear and elliptical wheel-rail contact cases.

Figure 27 shows the evolution of stresses and strains versus axle load on the critical plane in the case of a linear wheel-rail contact. Determining which factor predominantly contributes to fatigue damage on the critical plane is essential. If the maximum normal stress is negative or zero under rolling and sliding conditions, it indicates that damage is predominantly governed by shear stresses. Conversely, when the maximum normal stress is not insignificantly small, a detailed examination of failure mechanisms at crack initiation, considering both damage components, becomes necessary.

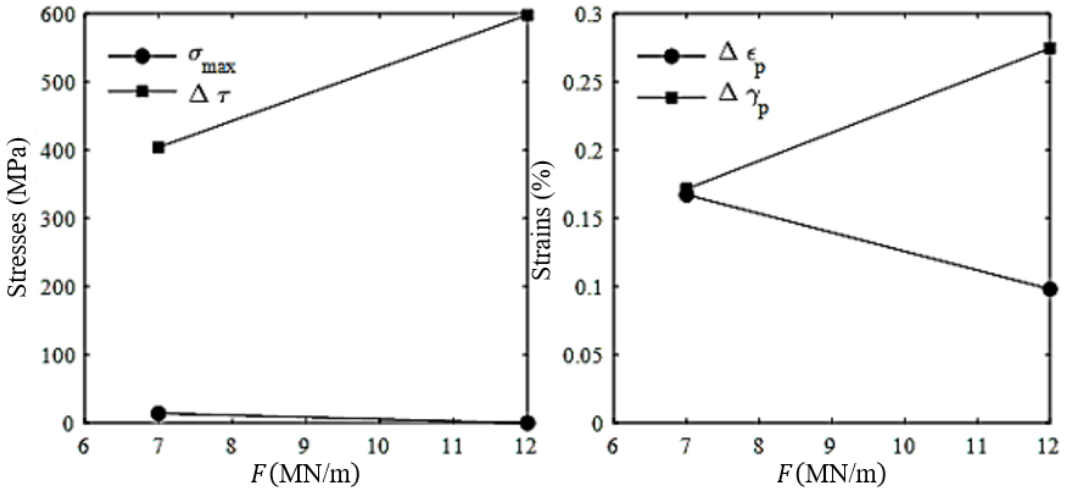

Figure 27: Evolution of stresses and strains versus axle load on the critical plane in the case of linear wheel-rail contact.

Figure 28 shows the evolution of damage FP_{tot} and its components FP_{I} and FP_{II} in the case of a linear wheel-rail contact. It can also be seen that FP_{max} is more strongly influenced by shear than by tension for $F = 7$ and 12 MN/m. Indeed, the evolution of the two damage components characterizing the failure modes due to the normal and shear components of stresses and strains, shows that FP_{I} is very low compared to FP_{II} for $F = 7$ and 12 MN/m. This suggests that damage is governed by shear.

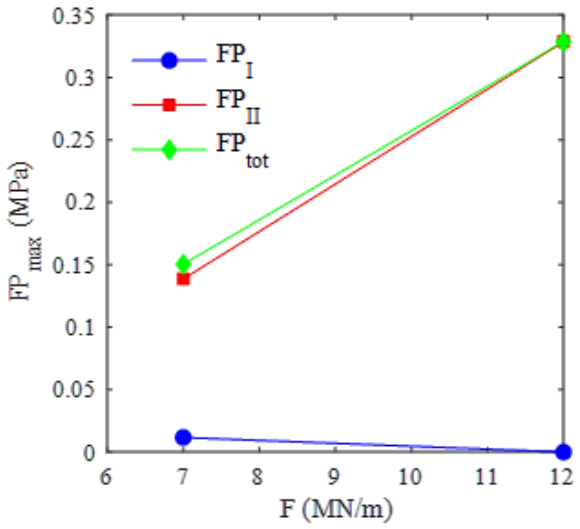

Figure 28: Evolution of damage and its contributions in the case of linear wheel-rail contact.

It should be noted that total damage increases with increasing axle load in both the linear and elliptical wheel-rail contact cases, as shown in Figure 29. Moreover, there is little difference between the linear and elliptical cases for $F = 7$ and 12 MN/m.

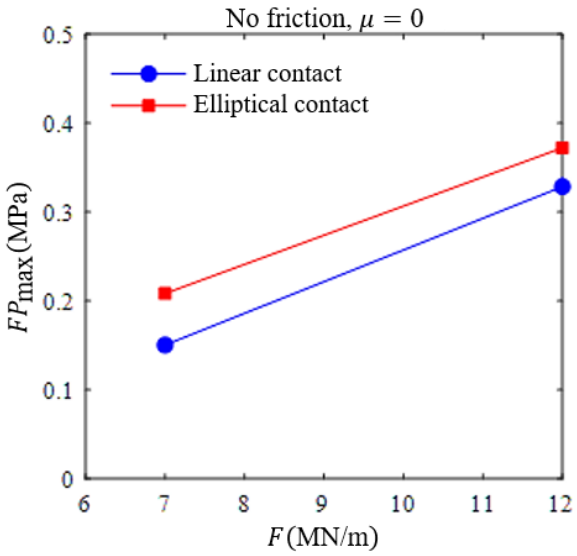

Figure 29: Evolution of damage versus axle load in the linear and elliptical wheel-rail contact cases.

6.4 Material critical plane

The plane with the highest maximum fatigue parameter within the wheel section is identified as the critical plane. Figure 30 shows the critical plane orientation angle versus axle load in the linear and elliptical wheel-rail contact cases. It can be observed that as axle load increases, the critical plane inclines relative to the rolling direction by 116 and 96 ° respectively for $F = 7$ and 12 MN/m in the case of linear wheel-rail contact, and by 151 and 71 ° respectively for $F = 7$ and 12 MN/m in the case of elliptical wheel-rail contact.

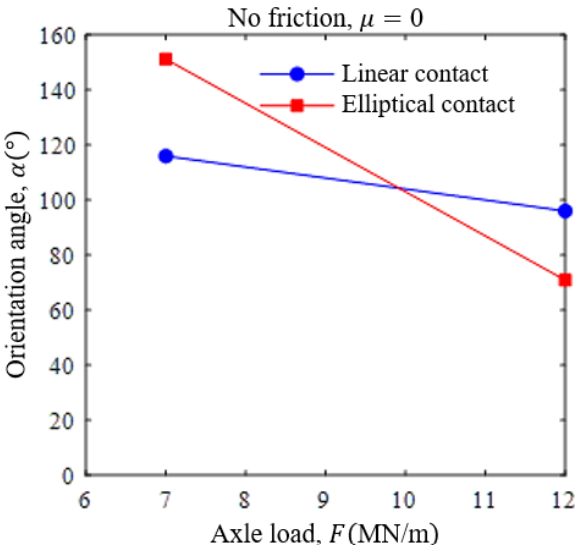

Figure 30: Evolution of the critical plane angle versus axle load in the linear and elliptical wheel-rail contact cases.

6.5 Fatigue life

Low-cycle fatigue life is primarily influenced by normal or shear strain, while stress becomes the dominant factor in fatigue life at higher cycle counts. Transition cycles between low- and high-cycle fatigue regimes typically fall within the range of 10^3 to 10^4 cycles to failure [15]. Moreover, tensile and shear cracking play a critical role in determining and governing the fatigue life. The fatigue life, denoted as N_f, at the FCR crack initiation is determined using Smith-Watson-Topper's law, from Equation (2). Figure 31 shows the evolution of fatigue life versus axle load in the linear and elliptical wheel-rail contact cases. It indicates that as axle load increases, the fatigue life of the wheel diminishes. Moreover, the fatigue life of the railway wheel also depends on the wheel-rail contact conditions. In existing literature, many researchers have taken a linear wheel-rail contact as a common assumption. Under linear contact conditions, the fatigue life of the railway wheel is notably longer compared to elliptical contact conditions. However, in realistic railway applications, wheel-rail contact is predominantly considered elliptical.

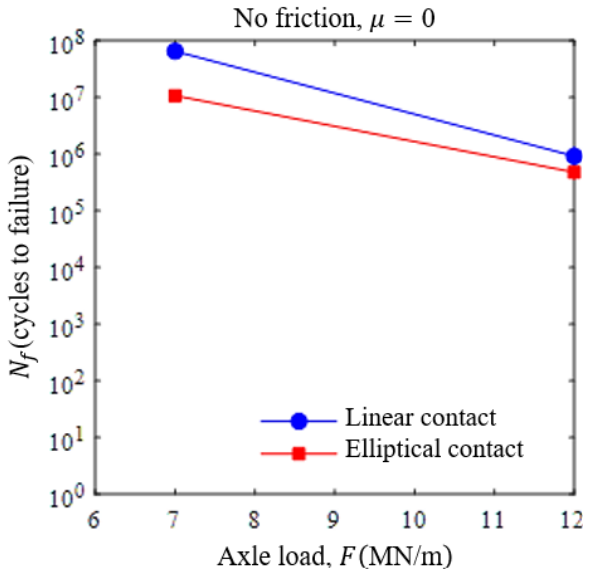

Figure 31: Evolution of fatigue life versus axle load with no friction in the linear and elliptical wheel-rail contact cases: p_0 (elliptical) $> p_0$ (linear), so $FP_{\max}$ (elliptical) $> FP_{\max}$ (linear), so N_f (elliptical) $< N_f$ (linear).

Table 6 gives the fatigue life values associated with various load levels, excluding the influence of friction at the wheel-rail interface in both linear and elliptical wheel-rail contact cases.

	F (MN/m)	
	7	12
Linear case	6.5×10^7	9.2×10^5
Elliptical case	1.1×10^7	4.8×10^5

Table 6: Calculated fatigue life at different load levels with $\mu = 0$, in the linear and elliptical wheel-rail contact cases.

7 Conclusion

In this article, Hertz's contact theory was used to analyze the geometric characteristics of the wheel-rail contact and the maximum contact pressures in this zone, considering two configurations: linear contact (cylinder-plane contact), which models the interaction between a railway wheel and a rail under certain simplified conditions, and elliptical contact (cylinder-cylinder contact with perpendicular axes), which corresponds to a more realistic modeling of wheel-rail contact in the railway context. The absence of friction at the wheel-rail interface has been taken into account.

The research findings demonstrate that the applied normal load, characterized by Hertz contact pressure, has a direct impact on the distribution of Von Mises residual stresses. In scenarios involving linear wheel-rail contact, the residual stresses are concentrated significantly beneath the contact surface. Conversely, in elliptical wheel-rail contact cases, an increase in axle load shifts this concentration closer to the contact surface, thereby elevating the potential risk for surface damage. Among the stress components observed, the normal stress σ_{11} has been identified as the most significant contributor to the stress distribution.

The location of equivalent plastic strain also varies according to contact configuration and applied load. At low axle loads, the behavior is predominantly elastic in both configurations. On the other hand, at higher loads, residual equivalent plastic strain appears on the surface, thus promoting the ratcheting effect (progressive accumulation of plastic deformation), a critical phenomenon that accelerates wear and threatens the integrity of railway components.

The analysis also highlighted the importance of the maximum fatigue parameter (FP_{max}), whose impact is more marked in the case of an elliptical contact than in a linear contact. The critical plane where FP_{max} manifests varies depending on the contact configuration. In addition, it was observed that material damage under cyclic loading is predominantly governed by shear stresses rather than tensile stresses within the pure rolling regime.

The study's plasticity model established a correlation between rising fatigue parameters ($FP_{\max}$) and diminishing wheel life (N_f). The multiaxial fatigue criterion utilized in this analysis has been shown to more accurately represent actual railway cyclic loading conditions compared to prior models, specifically the Dang Van model, which considered solely shear stresses.

The research has demonstrated that shear stresses are the primary factor in rolling contact fatigue (RCF) damage. Additionally, it has been observed that the nature of the wheel-rail contact, be it linear or elliptical, influences the stress concentration area and the progression of wear.

References

[1] Jay Prakash Srivastava, Prabir Kumar Sarkar, VR Kiran Meesala, and Vinayak Ranjan. Rolling contact fatigue life of rail for different slip conditions. *Latin American Journal of Solids and Structures*, 14(12):2243–2264, 2017.

[2] Xin Lizuo. Long-term behaviour of railway crossings: wheel-rail interaction and rail fatigue life prediction. *Delft University of Technology*, 2017.

[3] Heinrich Hertz. Über die berührung fester elastischer körper. *Journal für die reine und angewandte Mathematik*, 92:156–171, 1881.

[4] Kenneth Langstreth Johnson. *Contact Mechanics*. Cambridge University Press, 1987.

[5] Olgierd Cecil Zienkiewicz, Robert Leroy Taylor, , and Jian Z. Zhu. *The Finite Element Method: Its Basis and Fundamentals*. Elsevier, 2005.

[6] F. Braghin et al. Modeling the dynamics of railway vehicles. *Proceedings of the Institution of Mechanical Engineers, Part F: Journal of Rail and Rapid Transit*, 220(4):403–418, 2006.

[7] A. Kapoor. Shakedown of elastic-plastic structures: a review of the theory and its applications. *Archives of Mechanics*, 46(5):365–384, 1994.

[8] Kabo Elena and Ekberg Anders. Fatigue initiation in railway wheels—a numerical study of the influence of defects. *Wear*, 253(1-2):26–34, 2002.

[9] Jiang Yanyao and Sehitoglu Huseyin. A model for rolling contact failure. *Wear*, 224(1):38–49, 1999.

[10] Ringsberg Jonas W. *Rolling contact fatigue of railway rails with emphasis on crack initiation*. PhD thesis, Department of Solid Mechanics, Chalmers University of Technology, Göteborg, Sweden, 2002.

[11] Nemeyuko Médiateur. *Fatigue de contact de roulement*. PhD thesis, Université de Lorraine, 2023.

[12] Favrie Nicolas and Heuzé Thomas. Proposition de stage master recherche et/ou pfe modélisation eulérienne de l'écrouissage cinématique en grandes transformations pour la simulation de chocs. *Computational Structural Mechanics Association*, 2020.

[13] Saulot Aurélien. *Analyse tribologique du contact roue-rail Modélisation et expérimentations-Cas de l'usure ondulatoire*. PhD thesis, INSA-Lyon, 2005.

[14] ALACOQUE Jean-Claude and CHAPAS Pierre. Transport ferroviaire : gestion de l'adhérence. *Technique de l'ingénieur*, 2005.

[15] Azadi Mohammad. Failure analysis and prevention in powertrain systems. In *Handbook of Materials Failure Analysis with Case Studies from the Aerospace and Automotive Industries*, pages 471–492. Elsevier, 2016.